

1 Remote volcano monitoring using crowd-sourced imagery and Structure- 2 from-Motion photogrammetry: a case study of Oldoinyo Lengai's active pit 3 crater since the 2007-08 paroxysm

4 Pierre-Yves Tournigand¹, Benoît Smets^{1, 2}, Kate Laxton³, Antoine Dille², Lydéric France^{4, 5}, Gilles
5 Chazot⁶, Cristy Ho⁷, Christelle Wauthier^{7, 8}, Emma J Nicholson³, Charles Happe Kasanzu⁹, Maruvuko
6 Msechu¹⁰, Matthieu Kervyn¹

7 ¹ Department of Geography, Vrije Universiteit Brussel, Pleinlaan 2, 1050 Brussels, Belgium.

8 ² Department of Earth Sciences, Royal Museum for Central Africa, B-3080 Tervuren, Belgium.

9 ³Department of Earth Sciences, University College London, London, UK.

10 ⁴Université de Lorraine, CNRS, CRPG, F-54000 Nancy, France.

11 ⁵Institut Universitaire de France (IUF), France.

12 ⁶Université de Bretagne Occidentale, Brest, France.

13 ⁷Department of Geosciences, The Pennsylvania State University, USA.

14 ⁸Institute for Computational and Data Sciences, ICDS, The Pennsylvania State University, USA.

15 ⁹School of Mines and Geosciences (SoMG), University of Dar es Salaam, Tanzania, P.O. Box 35052

16 ¹⁰Tanzania Mining Commission P.O. Box 81, Dodoma, Tanzania

17 Corresponding author: Tournigand Pierre-Yves (pierre-yves.tournigand@vub.be)

18 Abstract

19 Active volcanic craters are highly dynamic geological features that undergo morphological changes on
20 a broad range of spatial and temporal scales. Such changes have implications for the stability of the
21 edifice, the eruptive style and the associated hazards. However, monitoring the morphological evolution
22 of active craters at high spatial resolution and over long periods of time can be challenging, especially
23 at remote volcanoes. In this study, we demonstrate the potential of Structure-from-Motion Multi-View
24 Stereo photogrammetry technique based on crowd-sourced data, applied to the case study of Oldoinyo
25 Lengai (OL) volcano in northern Tanzania. Following the 2007-08 paroxysm, OL volcano resumed its
26 characteristic effusive activity and started to fill in with lava the newly-formed 300 m wide and 130 m
27 deep pit crater. Monitoring capability is limited at OL due to its location in a remote non-urbanized area,
28 therefore, the eruptive and morphological evolution is poorly constrained (*e.g.*, lava emission rates,
29 number of vents, location of unstable areas), with hazard implications for tourists visiting the summit
30 area. Here we use crowd-sourced images, including Unoccupied Aircraft System (UAS) images,
31 ground-based videos and pictures collected between October 2014 and June 2022, to reconstruct high-
32 resolution topographic time-series of OL's summit crater. With these data, we have generated 7 Digital

33 Elevation Models (DEMs) of OL's pit crater spanning the past 8 years, and estimated the emitted volume
34 of lava and the corresponding time averaged discharge rates (TADR). From this we characterize the
35 geomorphological evolution of OL pit crater since the 2007-08 paroxysm and perform a preliminary
36 hazard assessment of the crater area. InSAR COSMO-SkyMed and Sentinel-1 data covering the periods
37 2013-2014 and 2018-2019 were also used in this study to complement our observations. Our results
38 indicate that the main location of lava emission within the crater floor has repeatedly shifted over the
39 years and that the 2008 cone has experienced a subsidence over time. OL's TADR has increased over
40 the years, reaching values one order of magnitude higher in the period 2021-2022 compared to 2014-
41 2018. Assuming similar TADR in the coming years, the crater could be filled in by lava within the next
42 decade, leading to new lava overflows on the flanks of the volcano.

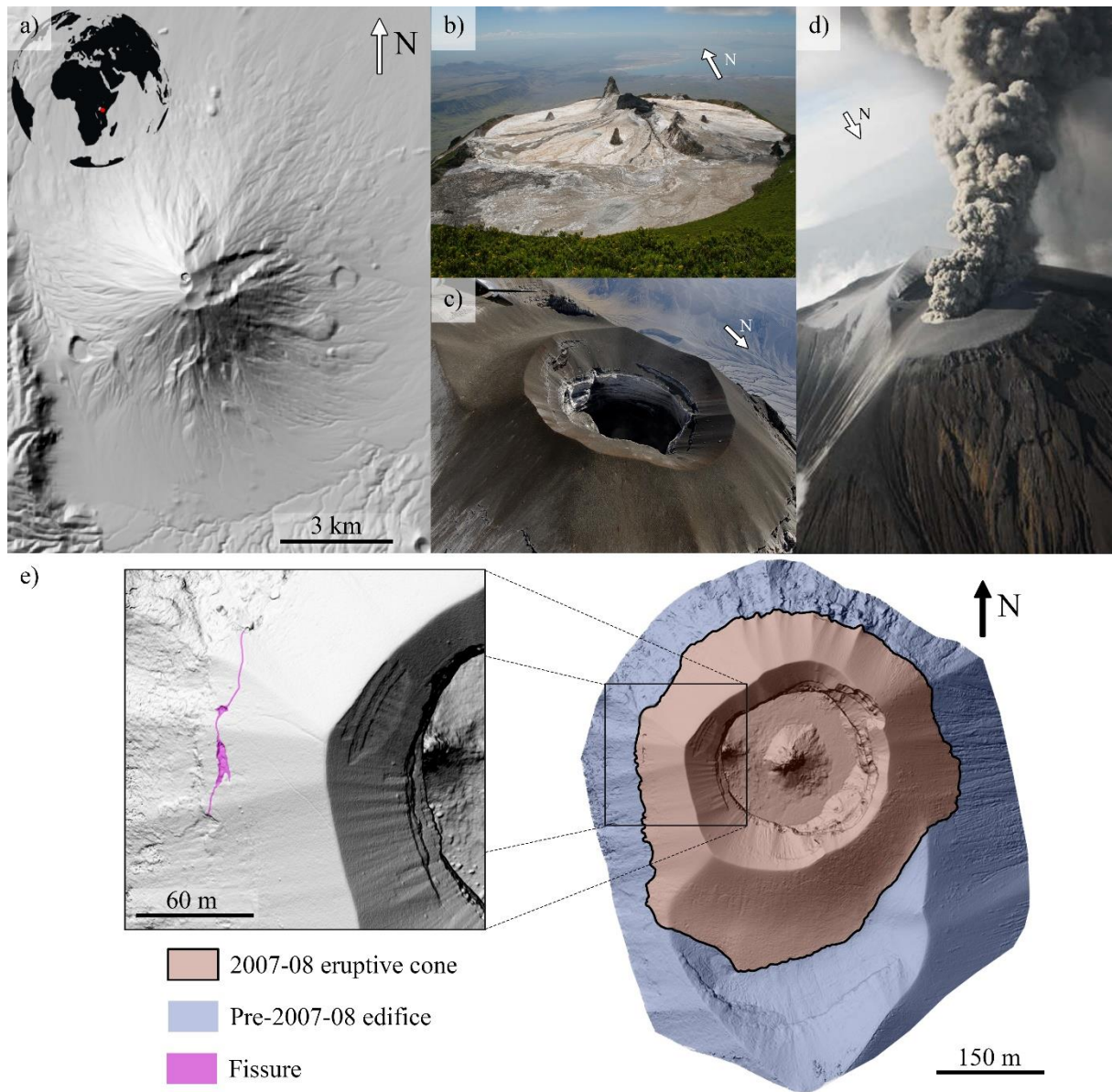
43 **Key words:** Crater morphology, Photogrammetry, UAS, Oldoinyo Lengai, Monitoring, DEM

44 **1. Introduction**

45 Active volcanic craters are highly dynamic geological features that undergo morphological changes over
46 a wide range of spatial and temporal scales (cm to km and hours to years, respectively). This topographic
47 evolution has many implications for the stability of the edifice, the eruptive style, and the location and
48 number of vents. Monitoring these changes is crucial to mitigate the numerous associated hazards, and
49 yet is challenging for remote volcanoes or small-scale morphological variations. As a consequence of
50 the development of automated Structure-from-Motion (SfM) and Multi-View Stereo (MVS) algorithms,
51 ground and airborne optical imagery are increasingly being used to generate high-resolution Digital
52 Elevation Models (DEMs), typically spanning spatial scales of a few square meters to several square
53 kilometers (*e.g.*, James and Robson, 2012; Civico et al., 2021; Dille et al., 2021; Schmid et al., 2021).
54 This approach is cost- and time-effective, and the spatial resolution and completeness of the DEMs
55 depend on the quality of the acquired data (*e.g.*, image spatial resolution, adequate lighting conditions,
56 number of images, geometry of acquisition, quality of camera-lens equipment) (Westoby et al., 2012;
57 Fonstad et al., 2013). The SfM-MVS technique has already been applied to develop numerical fluvial
58 models (*e.g.*, Javernick et al., 2016), to monitor the erosion of coastal cliffs (*e.g.*, James and Robson,
59 2012), to study landslides (*e.g.*, Lucieer et al., 2014; Dille et al., 2021), to characterize fault systems
60 (*e.g.*, Müller et al., 2017), and to describe geysers and geothermal systems (*e.g.*, Walter et al., 2020b).
61 It has also been used for active volcano monitoring, for example to track the evolution of volcanic domes
62 (*e.g.*, James and Varley, 2012; Darmawan et al., 2018; Zorn et al., 2020; Carr et al., 2022), dykes (*e.g.*,
63 Dering et al., 2019), lava flows (*e.g.*, James and Robson, 2014; Pedersen et al., 2022), or crater
64 morphology (Hanagan et al., 2020; Walter et al., 2020a; Civico et al., 2021). To the best of our
65 knowledge, only a few studies have used this technique to study the long-term morphological evolution
66 of active craters (*e.g.*, Derrien et al., 2015; Hanagan et al., 2020; Barrière et al., 2022) and even fewer
67 performed it on a crowd-source basis (*e.g.*, Snavely et al., 2008). In this study, the term crowd-sourced

68 data refers to open data provided by tourists and data shared through collaborations with scientists from
69 various fields working on OL volcano. Photogrammetry can provide crucial information on volcanic
70 activity evolution and facilitate the identification of future potential hazards (*e.g.*, lava overflow, crater
71 wall collapse, vent migration). Photogrammetric technique relies on image acquisition and is thus
72 applicable to both remote and highly dynamic environments, while being based on crowd-sourced data.
73 To demonstrate the benefits of such monitoring, we apply this technique to the case study of Oldoinyo
74 Lengai (OL) volcano, where series of images were acquired in the field by tourists and scientists without
75 aiming at performing photogrammetric surveys.

76 OL is a stratovolcano (2962 m a.s.l) located in northern Tanzania. It is the only active volcano in the
77 world to have emitted natrocarbonatite lavas historically (Keller et al., 2010). This type of emission has
78 been ongoing at OL for at least 11 ka (France et al., 2021). Since 1983, activity at OL volcano has mostly
79 been characterized by effusive lava emissions. However, on 4 September 2007, two explosive events
80 marked the beginning of a new eruptive phase that persisted until April 2008 (Figure 1). This new phase
81 was caused by a change in magma composition, from natrocarbonatite to nephelinite melt, and involved
82 short-lived explosive eruptions that generated volcanic ash plumes up to 15 km above vent at the peak
83 of activity (Keller et al., 2010; Kervyn et al., 2010; Bosshard-Stadlin et al., 2014). The direct
84 morphological consequence of this explosive phase was the formation of a pit crater, approximately 300
85 m wide and 130 m deep, in place of the lava platform that had filled the crater since 1983 (Kervyn et
86 al., 2010; Laxton, 2020). Following the 2007-08 paroxysm, the deep architecture and source of the
87 hydrothermal system has not drastically changed with respect to the pre-2007-08 paroxysm period
88 (Mollex et al., 2018). The normal effusive activity at OL resumed and has been filling the new crater
89 over the last 14 years, as reported through observations made sporadically by both scientists and tourists.
90 However, due to the remote location of the volcano (120 km away from the nearest city) and the lack of
91 scientific instruments on-site, there has been no permanent monitoring of OL's activity and crater
92 morphology evolution. Fortunately, the uniqueness of OL volcano's natrocarbonatite as well as the
93 neighboring points of interest (*e.g.*, Ngorongoro Lengai Geopark, Lake Natron) attract some tourists and
94 scientists in the area, generating valuable – though relatively rare - sources of data.

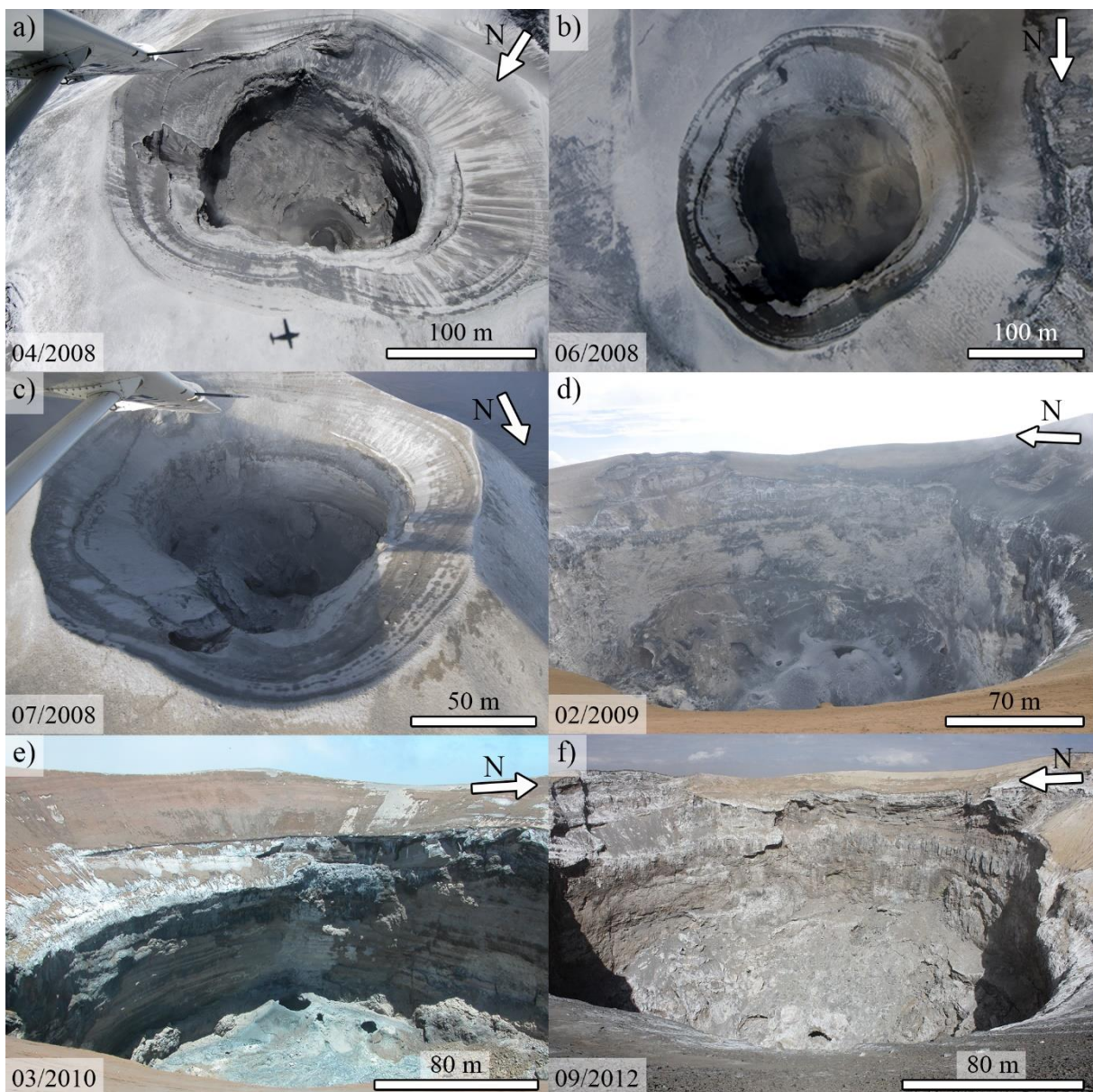


96

97 *Figure 1: Oldoinyo Lengai's a) location and hillshade of 30 m resolution SRTM DEM with overlap of July 2019 high resolution*
 98 *crater DEM, b) crater in May 2006 (Courtesy of Matthieu Kervyn), c) crater after the main explosive phases in March 2008*
 99 *(Courtesy of Benoit Wilhelmi), d) picture of one of the main explosive phases in February 2008 (Courtesy of Benoit Wilhelmi),*
 100 *e) January 2021 DEM of OL summit cone, inset highlights the fissuring process on the west external slope of the cone.*

101 Sporadic reports by tourists and visiting scientists, although mostly based on qualitative observations,
 102 provide useful information on the state of OL's activity and morphological evolution of the 2008 cone
 103 (Figure 2). Frequent eruptive activity, characterized by small-scale intra-crater lava flows and pools, has
 104 been observed since early 2009 (Global Volcanism Program, 2013a). The formation of hornitos and the
 105 occurrence of partial crater wall collapses have also been reported (Global Volcanism Program, 2008,
 106 2009). Crater depth has been estimated visually using a handheld laser in 2008 (130 m) and 2010 (120
 107 m), and through photogrammetric reconstruction in 2017 (100-125 m) (Global Volcanism Program,
 108 2008, 2010, 2018). However, these sparse data points do not allow for a quantitative analysis of the

109 evolution of OL's crater and overall cone structure, and therefore of the intra-crater lava accumulation,
110 eruption rates and surface displacements. In the absence of continuous in situ monitoring, multi-
111 temporal high-resolution topographic reconstructions, using ground-, drone-, and aircraft-based images
112 acquired by scientists, tourists, and pilots represent an invaluable source of data to retrieve OL's crater
113 evolution. The difficulties in obtaining high-resolution DEMs from satellite data due to regular cloud
114 cover and the small scale of the crater (≈ 300 m diameter) and its vent structures with respect to metric
115 satellite data resolution further emphasize the need for more creative solutions to data acquisition. Also,
116 higher precision measurements, such as ground-based Lidar, are not available for the period of interest.
117 Consequently, as a complement to photogrammetric data, Interferometric Synthetic Aperture Radar
118 (InSAR) show potential to monitor the surface displacements of the 2008 cone structure.



119

120 *Figure 2: Picture time-series from April 2008 to September 2012. Pictures a), b) and c) are airborne pictures acquired in*
121 *April, June and July 2008, respectively (Courtesy of Benoit Wilhelmi). d) February 2009 ground-based picture (Courtesy of*

122 *Ben Beeckmans*). *e) March 2010 ground-based picture (Courtesy of David Sherrod). f) September 2012 ground-based picture*
123 *(Courtesy of Franck Mockel).*

124 In this study, we demonstrate the capability of crowd-sourced photogrammetry to reconstruct a high-
125 resolution topographic time-series of the changing summit crater morphology of OL. From this time-
126 series, we characterize the geomorphological evolution of the summit crater of OL since the 2007-08
127 paroxysm and assess the hazard implications. For this, we collated several sources of optical images
128 including Unoccupied Aircraft Systems (UAS) images, videos and ground-based pictures that have been
129 collected by scientists or tourists between October 2014 and June 2022 (Figure 3). Using these diverse
130 datasets, we generated 7 DEMs of OL's pit crater spanning the past 8 years and estimated the lava
131 emitted volume and Time Averaged Discharge Rates (TADR) over time (Harris et al., 2007).
132 Additionally, InSAR data allowed to estimate the larger scale surface displacements related to the 2008
133 cone.



134

135 *Figure 3: Picture time-series from October 2014 to June 2022. a) October 2014 ground-based picture (Courtesy of Dr. France*
 136 *and Prof. Chazot), b) November 2017 UAS-based picture (Courtesy of Prof. Kervyn), c) and d) August 2018 and February*
 137 *2019 UAS-based pictures, respectively (Courtesy of P. Marcel and M. Caillet), e) July 2019 UAS-based picture (Courtesy of*
 138 *Dr. Laxton and Dr. Nicholson), f) January 2021 UAS-based picture (Courtesy of M. Dalton-Smith and G. Schachenmann), g)*
 139 *June 2022 ground-based picture (Courtesy of S. Chermette).*

140

2. Methodology

141

2.1. Data acquisition

142 One of the main challenges of this study was to gather a sufficient number of high-quality images for a
 143 given period in order to reconstruct a complete DEM of OL's active crater. The data are collated from
 144 6 different sources and allowed the reconstruction of 7 DEMs spanning more than 8 years. The sensors
 145 and acquisition methods vary greatly and include pictures and videos obtained using both UAS and
 146 ground-based Digital Single Lens Reflex cameras. The motivations for each data acquisitions were also
 147 quite diverse. Some images were taken by tourists (*e.g.*, 2018), others by scientists with the objective of
 148 performing 3D reconstructions of the active crater (*e.g.*, 2017 and 2019), and some for film-making
 149 purposes (*e.g.*, 2021). UAS data were obtained by flying over and within the pit crater. Ground-based
 150 data were mostly acquired from the crater rim, except in 2014 when a GoPro camera, fixed on a cable
 151 going across the crater, was used to descend inside the structure.

152 Various media sources were explored to collect these datasets. First, Global Volcanism Program bulletin
 153 reports for OL were reviewed to identify individuals who had climbed or flown over the crater since
 154 2008. Each person was contacted individually to assess those with potentially useful data for
 155 photogrammetric reconstruction. Additionally, extensive research was carried out on social media
 156 platforms (*e.g.*, YouTube, Facebook, Twitter) to identify other individuals or groups who had visited
 157 for tourism. The collected data were sorted and some periods were not used due to insufficient numbers
 158 of pictures (*i.e.*, 2008, 2010 and 2012, Figure 2). Detailed information on the data used to reconstruct
 159 the 7 OL DEMs are presented in Table 1.

Table 1: Properties of the pictures used for DEM reconstructions

| Year | Month | Dates | Cameras | Nb pictures | Resolution (px) | GPS geotagging | Source | Institution |
|------|-------|----------|--------------------------------|-------------|-----------------|----------------|--|---|
| 2014 | Oct | 12 to 14 | GoPro Hero3+ Black edition | 46 | 1920×1080 | No | Dr. France and Prof. Chazot | Université de Lorraine and Université de Bretagne Occidentale |
| | | | Nikon D7000 | 12 | 4928×3264 | | | |
| | | | <i>Information unavailable</i> | 8 | 4000×3000 | | | |
| | | | Kodak EasyShare DX7590 | 14 | 2576×1716 | | | |
| 2017 | Nov | 29 to 30 | DJI Phantom 4 | 344 | 1920×1080 | No | Prof. Kervyn | Vrije Universiteit Brussels |
| 2018 | Aug | 4 | DJI Mavic Pro | 151 | 1920×1080 | No | Patrick Marcel and Marc Caillet | - |
| 2019 | Feb | 28 | DJI Mavic Pro | 190 | 1920×1080 | No | | |
| 2019 | Jul | 29 to 31 | DJI Phantom 3 Pro | 146 | 4000×3000 | Yes | Dr. Laxton and Dr. Nicholson | University College London |
| | | | Canon PowerShot SX740 HS | 79 | 5184×3888 | | | |
| 2021 | Jan | 24 | DJI Mavic 2 Pro | 80 | 5472×3648 | Yes | Michael Dalton-Smith and Gian Schachenmann | - |
| 2022 | Jun | 24 to 27 | DJI Mavic Pro | 93 | 4000×2250 | Yes | Sylvain Chermette | - |
| | | | Sony Alpha 7 III | 64 | 6000×4000 | | | |

160

161 2.2. Data processing

162 Some images had to be extracted prior to the 3D reconstructions. Part of the data for the years 2014,
 163 2017, 2018 and 2019 were video-based, recorded using UAS or hand-held cameras. Frames were
 164 extracted from the videos and a selection made to ensure as many different viewing geometries and as
 165 much images overlap as possible on a case by case basis.

166

2.2.1 Photogrammetric 3D reconstruction

167 The 3D reconstruction was performed using Agisoft Metashape Pro v. 1.7.2 (AMP), a SfM-MVS
168 photogrammetry software. The reconstructions were obtained following the procedure described in
169 James and Robson (2014), James et al (2017) and Delhaye and Smets (2021). The first processing step
170 is an image quality control to detect and remove images that would negatively impact the quality of the
171 3D reconstruction (*e.g.*, blurred and badly exposed images). The AMP image quality estimation tool
172 was used for that purpose, and all images having a score lower than 0.7/1 were discarded. The value
173 provided by this tool is based on the sharpness level of the most in-focus part of the picture. An image
174 with a score inferior to 0.5/1 is recommended to be excluded from the data processing by the AMP user
175 manual. This 0.7/1 threshold was arbitrarily set to improve the quality of the dataset while avoiding
176 missing the necessary image overlap and view angles to perform a proper 3D reconstruction.

177 The next step is the image alignment, *i.e.*, image matching and interior/exterior orientation estimation.
178 The output is a point cloud made of tie points (*i.e.*, points visible on at least two images), called sparse
179 point cloud (SPC), and the estimation of the interior orientation parameters, called “camera calibration”
180 in AMP. To improve the interior/exterior orientation, the SPC was filtered using filtering options
181 provided by the software and an optimization of the camera calibration. These filters are based on
182 specific metrics that allow the operator to remove the less precise tie points. A full description of these
183 filters is provided in the AMP user manual (<https://www.agisoft.com/downloads/user-manuals/>).

184 After georeferencing (see 2.2.2), a dense matching is performed to produce a dense point cloud (DPC)
185 representing the full 3D reconstruction product. The DPC is eventually cleaned up manually on its edges
186 and where clusters of useless points are located. The cleaned DPC of each available periods (epoch) is
187 finally used to produce a DEM (Figure 4). Further processing information are available in the table S1
188 of the supplementary material.

189

2.2.2 Georeferencing

190 None of the 7 datasets included ground control points (GCPs) and 4 had no associated GPS data, yet
191 georeferencing is essential for cross-model comparison. To perform such comparison, we used a
192 reference epoch having a good quality of image acquisition and geotagging information. The precision
193 of this geotagging is equivalent to a unique consumer-grade GNSS receiver (*i.e.*, 5 to 10 m), but provides
194 centimeter- to decimeter-scale precision for an accurate scaling of the model. The reference epoch is the
195 July 2019 dataset. It offers the best spatial resolution available in the time-series, with images acquired
196 during ideal lighting conditions (*i.e.*, no extreme light-shadow contrasts, good visibility and exposure
197 highlighting well the ground surface texture). As the type of image, geometry of acquisition and
198 conditions of illumination significantly differ between epochs, multi-epoch co-alignment during the
199 photogrammetric processing, as commonly suggested for an accurate co-registration (*e.g.*, Feurer and
200 Vinatier, 2018; Hendrickx et al., 2020; Delhaye and Smets, 2021), was not possible. Consequently, we

201 used the fully processed reference epoch July 2019 to manually extract the coordinates of 10 reference
 202 points visible in the final 3D products and use these points as GCPs for the other epochs. Each of these
 203 points is associated with a recognizable feature within OL’s crater that could be identified easily in all
 204 the other epochs. It allowed for a co-registration of all available epochs in our dataset.

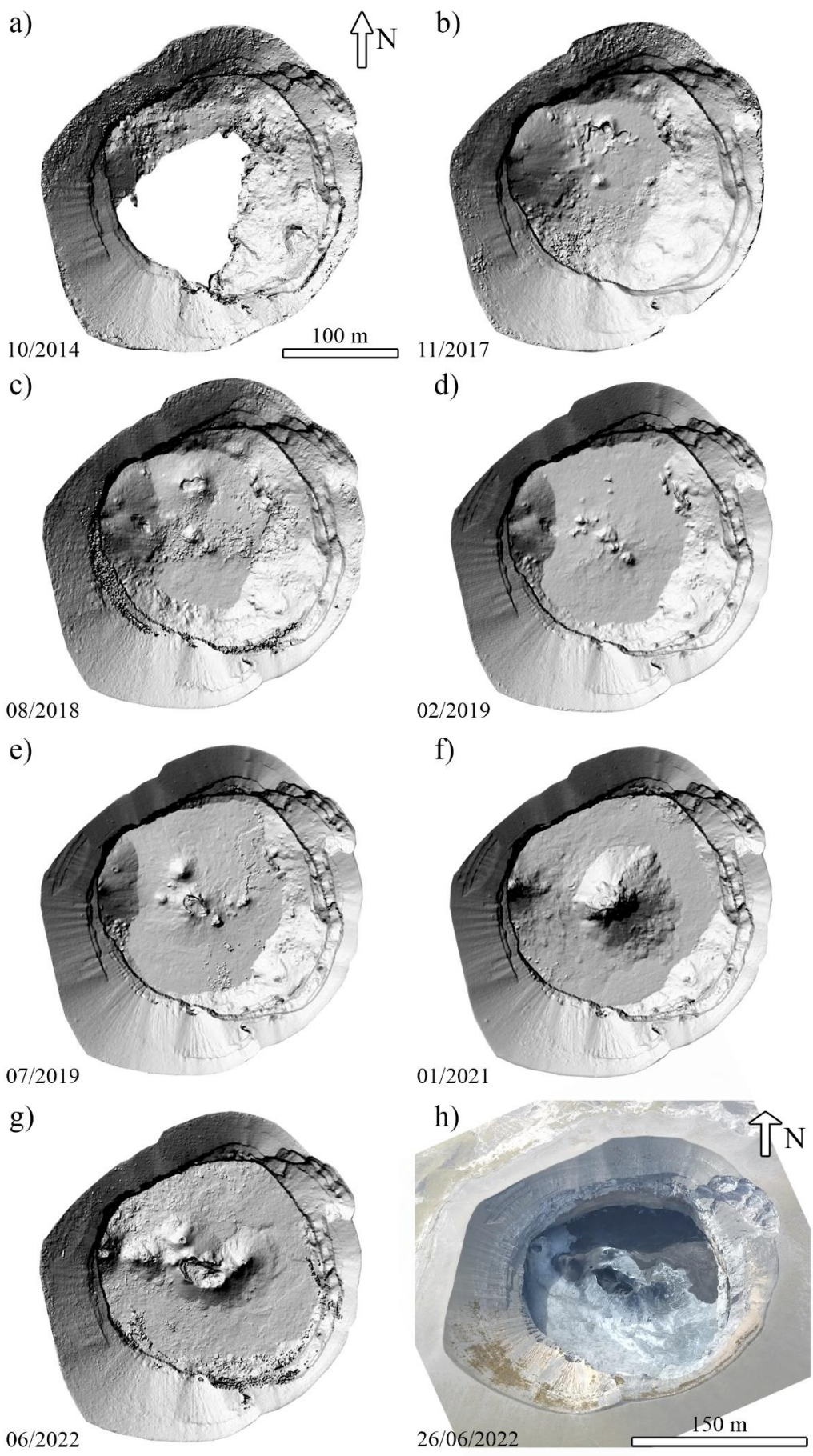
205 To assess the quality of the co-registration, we used the CloudCompare M3C2 plugin (Lague et al.,
 206 2013; Girardeau-Montaut, 2016). For each DPC, regions assumed to be stable around the crater were
 207 selected and compared to the reference July 2019 model. These DPC samples correspond to cone slopes
 208 with no evidence of volcanic activity (*e.g.*, tephra accumulation, collapse) or vegetation. The use of cone
 209 slopes to assess the co-registration enables both vertical and horizontal registration (Delhaye and Smets,
 210 2021). Results are reported in table 2.

211 All the co-registration differences are between 0.1 and 1.1 m with an average standard deviation of 0.3
 212 m. These results indicate that all elevation changes measured between DEMs superior to 1.5 m are
 213 significant and correspond to real elevation changes in the pit crater. This value is conservative and is
 214 lower for all dates but August 2018.

Table 2: 3D reconstruction properties

| DEM | Ground resolution (cm/px) | RMS reprojection error (m) ^(a) | Max reprojection error (m) | Average co-registration difference (m) | Average co-registration standard deviation (m) |
|----------|---------------------------|---|----------------------------|--|--|
| 2014 | 13.88 | 0.22 | 5.31 | 0.11 | 0.51 |
| 2017 | 23.76 | 0.34 | 18.33 | 0.73 | 0.31 |
| 2018 | 20.97 | 0.20 | 6.30 | 1.11 | 0.38 |
| 2019 Feb | 28.93 | 0.17 | 2.05 | 0.46 | 0.24 |
| 2019 Jul | 11.87 | 0.25 | 0.89 | NaN | NaN |
| 2021 | 21.36 | 0.21 | 0.70 | 0.40 | 0.22 |
| 2022 | 18.54 | 0.21 | 0.56 | 0.64 | 0.39 |

(a) The RMS reprojection error is provided by the Agisoft Metashape software and correspond to the root mean square of normalized reprojection error.



216 *Figure 4: Overview of the 7 DEMs reconstructed in this study: a) October 2014, b) November 2017, c) August 2018, d)*
217 *February 2019, e) July 2019, f) January 2021, g) June 2022. The bottom right picture, taken on 26th of June 2022, shows the*
218 *current state of OL's crater morphology (Courtesy of Sylvain Chermette).*

219 **2.2.3 Depth and volume change estimates**

220 Parameters related to the morphology of the crater (*e.g.*, depth, surface, volume) as well as to the
221 dynamics of the activity have been extracted from the DEM time-series (Figure 4).

222 The DEMs were subtracted from each other to map the elevation differences across the entire crater area
223 (Figure 5) allowing both a qualitative and quantitative appraisal of OL crater morphological evolution.

224 As OL crater rim elevation is constant in time but variable around the crater, with minimum and
225 maximum elevation around 2887 and 2908 m in the W-NW and S-SE area respectively, the average rim
226 altitude (2895 m) was retrieved from the July 2019 reference model and used as the crater rim elevation.

227 The crater depth has been retrieved by manually contouring and measuring the average elevation of the
228 young lava platform (*i.e.*, crater floor elevation) in each DEM, which was then subtracted from the
229 average crater rim elevation.

230 The crater volume is the volume of lava needed to completely fill OL's crater. This parameter was
231 obtained by measuring the empty volume below a virtual platform at the average crater rim elevation..

232 Using the obtained crater volume, we derived the TADR in m³/month:

$$233 \quad TADR = \frac{|V_2 - V_1|}{t_2 - t_1} \quad (1)$$

234 with V_2 and V_1 being the crater volumes of two successive epochs and $t_2 - t_1$ the time difference between
235 the two epochs of interest.

236 In order to retrieve the error associated to Volume and TADR calculations it was first necessary to verify
237 the error distribution in the M3C2 results. Quantile-Quantile (Q-Q) plots were used to identify potential
238 deviation from a normal distribution (supplementary material Figure S1). A strong deviation from a
239 straight line was observed indicating a non-normal distribution of the error. We thus followed the same
240 procedure as in Höhle and Höhle, (2009) and Pedersen et al., (2022) consisting in using the Normalized
241 Median Absolute Deviation (NMAD) an estimate for standard deviation less sensitive to outliers in the
242 datasets, to estimate the error associated to Volume and TADR estimates:

$$243 \quad \sigma_V = A \cdot NMAD \quad (2)$$

244 where σ_V is the Volume uncertainty and A is the area that experienced an elevation change.

$$245 \quad \sigma_{TADR} = \frac{A}{t_2 - t_1} \sqrt{NMAD_1^2 + NMAD_2^2} \quad (3)$$

246 where $t_2 - t_1$ is the time difference between 2 DEMs.

247

2.3. Surface displacements (InSAR data)

248 Surface displacements have also been quantified using InSAR to provide insights on the larger scale
249 motion of the 2008 cone. Surface displacements were quantified using differential InSAR on three SAR
250 datasets: 100 descending COSMO-SkyMed X-band (wavelength = 3.1 cm) SAR images spanning 2
251 February 2013 – 28 November 2014 provided by the Italian Space Agency (ASI), 35 descending
252 Sentinel-1 C-band (wavelength = 5.55 cm) SAR images spanning 21 July 2018 – 12 January 2020, and
253 44 ascending Sentinel-1 C-band SAR images spanning 25 July 2018 – 4 January 2020 provided by the
254 Alaska Satellite Facility (ASF). The COSMO-SkyMed dataset was multi-looked at 5 looks in range and
255 5 looks in azimuth, while the Sentinel-1 datasets were multi-looked at 10 looks in range and 2 looks in
256 azimuth. 510 descending COSMO-SkyMed interferograms were made using a baseline threshold of 200
257 m and a maximum of 200 days between acquisitions. A baseline threshold of 300 m and a temporal
258 threshold of 50 days were used to generate 95 descending and 162 ascending Sentinel-1 interferograms.
259 Differential InSAR processing and unwrapping were completed using the GAMMA software (Werner
260 et al., 2000). Topographic phases were removed using a digital elevation model of OL edifice with a 12
261 m spatial resolution from TanDEM-X (Krieger et al., 2007).

262 Cumulative surface displacement maps and time-series of displacements were generated using the
263 Multidimensional Small Baseline Subset (MSBAS) version 3, a software that uses the least squares
264 method on a differential InSAR dataset to produce one-dimensional Line-Of-Sight (LOS) time-series,
265 or a combination of ascending and descending datasets to produce two-dimensional, vertical and
266 horizontal east-west, time-series (Samsonov, 2019). Compared to conventional InSAR, MSBAS can
267 detect smaller ground displacements over longer timespans and has been successfully used to analyze
268 deformation related to volcanic processes (Samsonov and d'Oreye, 2012; Smets et al., 2013; Stephens
269 and Wauthier, 2022; Gonzalez-Santana et al., 2022). The areas of interest at the crater were sampled at
270 10 x 10 pixels (120 m x 120 m). The InSAR time-series reference (10 x 10 pixels) is centered on the
271 location of the OLO3 GPS station (-2.754°, 35.871°) from the TZVOLCANO GNSS Network (Stamps
272 et al., 2016). The location is relatively stable based on GPS time-series spanning 2016-2021, which is
273 detrended using MIDAS (Blewitt et al., 2018) and available through the Nevada Geodetic Laboratory
274 database. No GPS data are available from 2013-2014, so we assume that the location of station OLO3
275 was also stable during this period for consistency.

276

3. Results

277 The explosive activity that took place between September 2007 and April 2008 excavated a 130 m deep
278 pit crater, around which a new pyroclastic cone formed and now sits atop the older active platform
279 (Figure 1c and e). The pyroclastic cone is easily distinguishable from the older structures due to its
280 smooth texture (Figure 1e). In this study, the pit crater within the cone is divided into two sections, a
281 steep-sided inner crater (\approx 200 m diameter) from the crater floor to 2866 m elevation that will be referred

282 to as the lower crater section and a wider upper section (≈ 300 m diameter) from 2866 to 2895 m
283 elevation with a slope mainly at the repose angle with an average angle of 33° , referred to as the upper
284 crater section (Figure 6a). The lower crater section is approximately circular while the upper crater
285 section is slightly elongated in the NE-SW direction. The upper crater section displays several features
286 on the inner eastern slopes corresponding to collapses that occurred in the months following the
287 paroxysm (Figure 2). On the external section of the cone, one of the most noticeable features on our
288 DEMs is the ≈ 100 m long fissure running parallel to the cone base on the western slopes (Figure 1e).

289 Since 2014, OL's crater has undergone further significant morphological changes, including progressive
290 filling of the crater with new lava, hornitos growth and collapses, and partial collapses of the crater walls
291 (Figure 5). We describe the main features of each of these processes in the sections below. For clarity,
292 vents or clusters of vents are referred to using an associated number (*e.g.*, V1, V2,...; Figure 5). When
293 a vent does not significantly change location or size, its name is carried out to the next time step. On the
294 other hand, if the location and/or dimension of a vent has changed, if several vents merged, or if vents
295 are visible in an area previously devoted of any vent then a new name is attributed to it.

296 **3.1. Crater filling**

297 **3.1.1 Lava field**

298 The progressive filling of the crater is clearly visible throughout the 2017 to 2022 reconstructed DEMs,
299 distinguishable from the smooth unaltered texture that the fresh lava generates (Figure 5, dashed purple
300 contours). In 2017, a young lava field is noticeable in the north and central part of the crater at a depth
301 of 110 m, relative to the average crater rim elevation (Figure 3b and Figure 5b). A large hornito in the
302 west (V1) and four main vents (V2-5) are identified, including a 12 m diameter lava pool (V2). In 2018,
303 the lava field displays a 27% increase in surface area and a 3-4 m increase in elevation (107 m depth)
304 with respect to 2017 (Figure 5c and Table 3). Several vents are observed, including a lava pool (V5) on
305 the eastern part of the field. The pool was active at the time of data acquisition. In both 2017 and 2018,
306 the active vents are located in the northern half of the lava field. From February 2019 onwards, all active
307 vents appear confined to the center of the lava field, which had expanded in area by 50% and increased
308 in elevation by 4-5 m (99 m depth) with respect to August 2018 (Figure 5d). A similar vent layout is
309 noticeable in July 2019 with 5 active structures (V12-16) developing in the center of the field (Figure
310 5e). The main structure (V14) consists of an elliptical pool measuring 24 x 14 m along its major and
311 minor axis, respectively. The lava field surface area expanded by a further 14% with respect to the
312 previous DEM, while its depth relative to the crater rim decreased to 97 m. Between July 2019 and
313 January 2021, the active vents continued to converge towards the center of the crater, resulting in the
314 formation of a single tall hornito (V17) measuring 55 m in height relative to the crater floor level (88 m
315 depth) (Figure 3f). A 30% increase in the lava field surface area is also observed during this time period
316 (Figure 5f). In June 2022, the main central hornito collapsed creating a E-W elongated lava pool (V17)

317 associated with several secondary vents (V18-21) aligned in the same orientation (Figure 5g). The lava
 318 field surface area increased by 14% and its average elevation reached 2822 m (73 m depth), almost
 319 entirely covering the remnants of V1 hornito. Cumulatively, between 2017 and 2022, the lava field
 320 surface increased from $8.4 \times 10^3 \text{ m}^2$ to $2.7 \times 10^4 \text{ m}^2$, while its average elevation rose by 37.2 m (from
 321 2785.2 to 2822.4 m, respectively). Furthermore, a west-east alignment of the active vents appears from
 322 2018 and remains visible until 2022.

323

Table 3: Parameters extracted from DEMs and field estimates

| Years | Depth (m) | Lava field area (m ²) | Crater volume (m ³) | σ_v (m ³) | TADR (m ³ /month) | σ_{TADR} (m ³ /month) | Months |
|----------|-----------|-----------------------------------|---------------------------------|------------------------------|------------------------------|--|--------|
| 2008 | 130* | NaN | 3.58E+06* | NaN | NaN | NaN | NaN |
| 2010 | 120* | NaN | 3.56E+06* | NaN | 9.60E+02* | NaN | 22 |
| 2014 | 115.7 | NaN | 3.52E+06 | 6.42E+03 | 6.00E+02 | NaN | 55 |
| 2017 | 110.3 | 8392 | 3.38E+06 | 4.60E+03 | 3.80E+03 | 1.98E+02 | 37 |
| 2018 | 106.7 | 10679 | 3.37E+06 | 3.02E+03 | 8.00E+02 | 6.85E+02 | 9 |
| 2019 Feb | 98.6 | 15887 | 3.31E+06 | 2.82E+03 | 1.10E+04 | 6.65E+02 | 6 |
| 2019 Jul | 96.8 | 18062 | 3.27E+06 | NaN | 8.40E+03 | NaN | 5 |
| 2021 | 87.8 | 23417 | 2.96E+06 | 7.81E+03 | 1.70E+04 | 4.34E+02** | 18 |
| 2022 | 73.1 | 26728 | 2.60E+06 | 1.73E+04 | 2.10E+04 | 1.13E+03 | 17 |

Note. Depth = Crater depth with respect to average lava platform and crater rim elevation, Crater volume = Volume available below a plane at the crater rim elevation, Months = number of months elapsed with respect to previous DEM, NaN = Not a Number (No data available). *2008 and 2010 depth values come from estimates determined by Chris Weber and Dr. David Sherrod, respectively (Global Volcanism Program, 2008, 2010). **This σ_{TADR} uncertainty value could not be calculated based on the described method and thus was obtained by dividing σ_v by the number of months elapsed between July 2019 and 2021 surveys.

324

325 3.1.2 Hornitos

326 A west emission center (V1) is noticeable in every DEM (Figure 5). V1 formed a hornito located against
 327 the western crater wall (Figure 5b). Between 2014 and 2017, this structure increased in volume, as
 328 shown by the yellow/orange color scale in Figure 5b. The volume change of the entire hornito cannot
 329 be constrained for each time period as the central lava field progressively covered the base of the hornito
 330 and some crater wall collapses exposed parts that were previously hidden. We therefore measured the
 331 change in the maximum height of the hornito's peak area between 2017 and 2022. From November 2017
 332 to August 2018, V1 falls by 3.5 m in maximum elevation (Figure 5b, c). These changes in elevation are
 333 accounted for by 2 collapses that can be distinguished in Figure 5c, one at the V1 summit and one on
 334 the eastern side closer to its base. Between August 2018 and February 2019, V1 decreased by a further
 335 2.3 m in maximum elevation. In July 2019, V1 exhibits an increase in maximum elevation of 5.3 m
 336 followed by an increase in maximum elevation of 24.8 m by January 2021 (Figure 5e and f). From
 337 January 2021, V1 continued to grow, albeit at a slower rate, however its maximum elevation dropped
 338 by 1.8 m by June 2022. Figure 5g shows that by June 2022 V1's summit has again collapsed and instead
 339 exhibits a growth around 10 m to the north.

340 Until February 2019, large scale hornitos and lava pools such as V2 ($> 1000 \text{ m}^2$) formed predominantly
341 in the northern part of the crater, while the central part only contained small-scale structures, such as
342 V3-12 ($< 300 \text{ m}^2$). All the vent structures were low in elevation relative to the average elevation of the
343 crater floor ($< 10 \text{ m}$). By February 2019, all vents were confined to the central part of the crater and
344 remained relatively small low elevation edifices (V9-12). From July 2019, larger structures developed
345 ($> 10 \text{ m}$), all in the central region of the crater. These structures included a large collapsed hornito (V14)
346 and several smaller ones (V12, 13, 15 and 16). Within the V14 collapsed structure, we observe several
347 active vents characterized by a notable E-W alignment. In all the DEMs presented in this study, no active
348 vent was observed in the southern part of the crater. By January 2021, all vents coalesced into one central
349 55 m tall hornito (V17) with a basal diameter of $\approx 90 \text{ m}$, for a total volume of $6.6 \times 10^4 \text{ m}^3$. The structure
350 subsequently collapsed, and 5 vents (V17-21) opened around it, forming a network of smaller scale
351 hornitos ($\approx 15 \text{ m}$ high; Figure 5g). From January 2021 onward, the vent structures (V17-21) grew further
352 to reach higher elevations ($> 20 \text{ m}$) compared to previous years and started resembling the structures
353 observed during the 2000-2008 period (Figure 1) (Kervyn et al., 2008).

354 **3.1.3 Crater volume evolution**

355 A time series of crater depth was obtained by measuring the average elevation of the young
356 natrocarbonatite lava platform in each DEM. In October 2014, a substantial portion of the lava field is
357 missing due to the incomplete DEM. In this case, the average elevation along the margin of the missing
358 area's contour was used as a depth estimate, assuming a horizontal topography. OL's crater depth has
359 been decreasing at different rates over time (Figure 6a). Two main trends are observed, one for the
360 period between October 2014 and August 2018 during which the crater depth decreased by $\approx 9 \text{ m}$,
361 corresponding to 0.2 m/month , and the second between August 2018 and June 2022, during which the
362 crater depth decreased by $\approx 34 \text{ m}$, corresponding to a higher rate of 0.7 m/month (Figure 6b).

363 The first trend is in good agreement with previous crater depth measurements acquired in 2010 (Global
364 Volcanism Program, 2010). Conversely, the depth value obtained in 2008 (Global Volcanism Program,
365 2008) appears higher than expected compared to the data presented here. However, one should
366 remember that, due to the cone-shaped morphology of the original crater following the 2007-08
367 paroxysm, it is expected that the crater depth decreased at a faster rate in the years immediately following
368 the resumption of effusive activity.

369 The remaining volume of the crater was measured for each available DEM using the average crater rim
370 elevation as a reference (Figure 6c). It is important to note that debris from crater wall collapses that
371 have occurred over the studied period fell inside the crater and consequently do not impact the overall
372 volume evolution estimation. Crater volumes were estimated at $3.5 \times 10^6 \text{ m}^3$ in 2014 compared to 2.6×10^6
373 m^3 in 2022 corresponding to a 26% volume decrease in 8 years. As for the crater depth, two evolution
374 trends are observed in the volume data. The first trend (from October 2014 to August 2018) shows that

375 the crater lost $\approx 4\%$ of its volume in almost 4 years. In comparison, the crater volume decreased by a
376 further 23% between August 2018 and June 2022. The TADR_s highlight the same two distinct
377 evolutions over time with an initial steady low emission ($< 6 \times 10^3 \text{ m}^3/\text{month}$) trend pre-2018 followed
378 by a constantly increasing trend reaching a maximum emission rate of $2.1 \times 10^4 \text{ m}^3/\text{month}$ by June 2022.

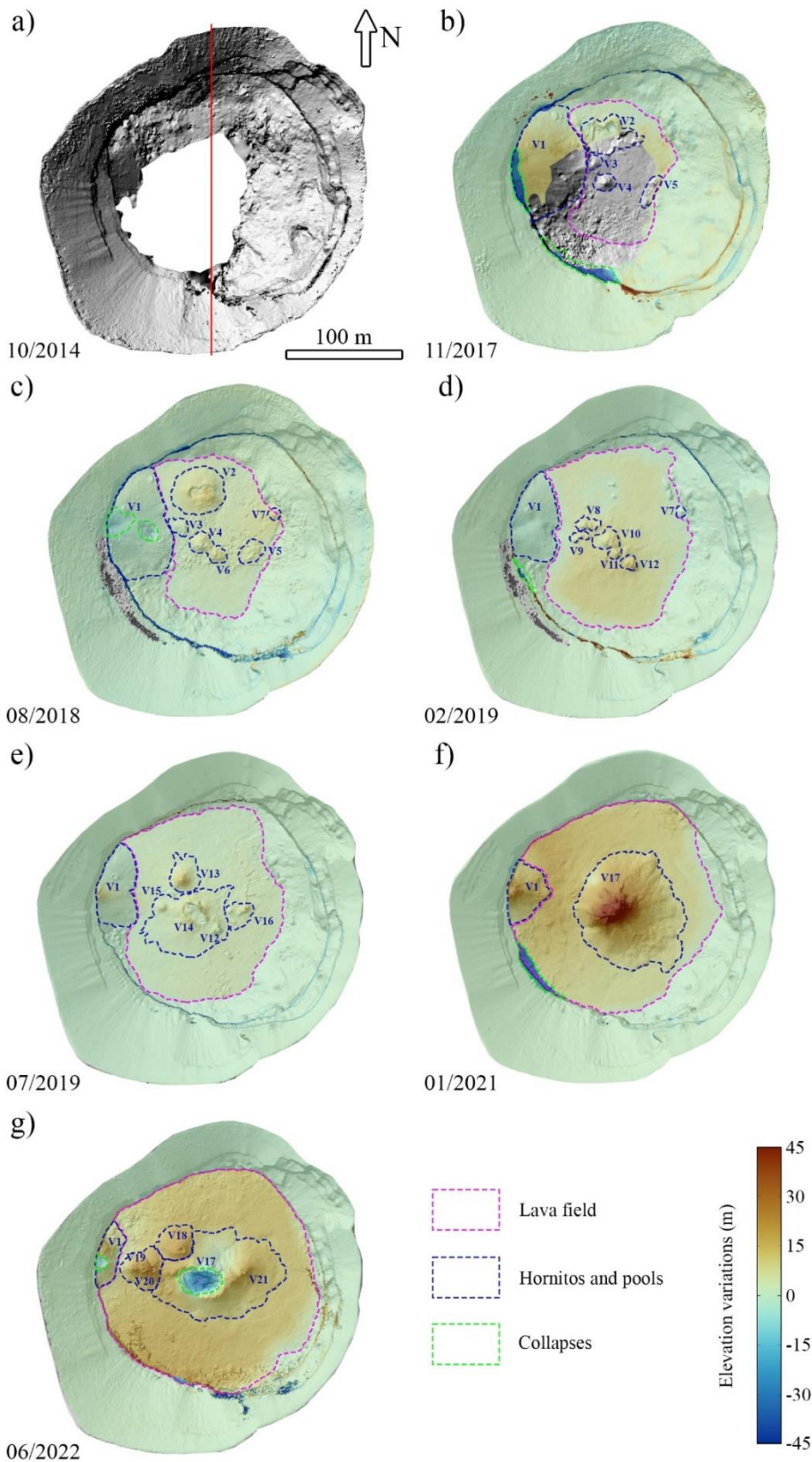
379 We estimated the pit crater volume for the years 2010 and 2008. In these years the floor of the pit crater
380 had a cone shape (Figure 2a and c) that got rapidly filled over time. In the absence of DEMs for these
381 years, the 2014 crater volume was used as a reference to which we added a supplementary volume
382 calculated separately. To calculate the 2010 supplementary volume, the average slope of the northern
383 region of the lower crater section was measured on the reconstructed 2014 DEM to be 27.3° . This slope
384 value was then used to derive a truncated cone volume (Figure 6a, blue dashed lines) below the 2014
385 lava field area. For 2008, a supplementary cone volume was added with a diameter equivalent to the
386 2010 truncated cone and a tip reaching the depth measured in 2008 (Figure 6a, dark blue dashed lines).
387 The corresponding TADR results showed in Figure 6c for the periods 2008-2010 and 2010-2014 are
388 consistent with a steady low emission period pre-2018.

389 **3.2. Collapses**

390 Several crater wall collapses occurred in 2017, February 2019 and 2021 (Figure 5, dashed green
391 contours). These collapses developed on the top of the lower crater section, in the west to south-west
392 sectors, at an average elevation of 2866 m. Each wall collapse is distinguished by the dark blue shaded
393 areas in figure 5, indicating an elevation change after the collapse greater than 45 m. This change agrees
394 with the altitude difference between the top of the lower crater section and the crater floor in the three
395 cases (81 m in 2017, 69 m in 2019 and 58 m in 2021). Furthermore, we observe the presence of meter-
396 size blocks on the crater floor below the collapsed area. These collapse areas extend several tens of
397 meters in length scale and appear to be restricted geographically to the southwestern walls of the lower
398 crater section.

399 **3.3. Cone subsidence**

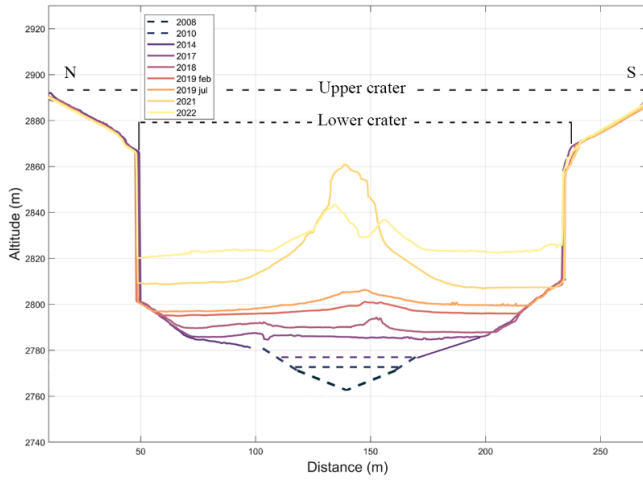
400 The InSAR data provided us with cumulative surface displacement maps supporting subsidence at the
401 cone relative to the surrounding area (Figure 7). LOS displacements of the northern (A) and southern
402 (B) flanks both have linear rates of -3.4 cm/year according to the descending COSMO-SkyMed dataset
403 spanning February 2013 – November 2014. Simultaneously processing the ascending and descending
404 Sentinel-1 datasets spanning July 2018 – January 2020 yields both vertical and horizontal displacements.
405 The northern (A), southern (B), western (C), and eastern (D) flanks have vertical displacement linear
406 rates of -2.0 , -1.0 , -1.3 , -0.6 cm/year , respectively, and horizontal displacement linear rates of -0.6 , -0.6 ,
407 -0.5 , -0.4 cm/year , respectively. The biannual cyclic patterns, which are especially apparent in the
408 vertical and horizontal displacement time-series, correspond to the wet seasons that occur in the periods
409 March – May and October – December, when the ground swells with rainwater (Rey et al., 2021).



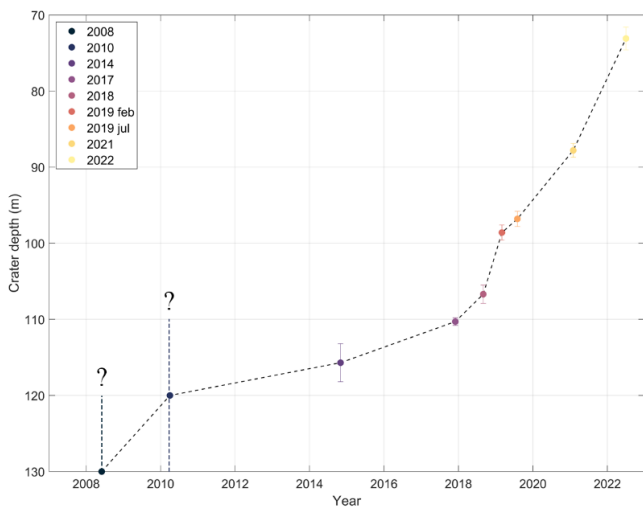
410

411 *Figure 5: Morphological evolution of OL's crater obtained by DEM subtraction: a) October 2014 DEM, b) November 2017 –*
 412 *October 2014, c) August 2018 – November 2017, d) February 2019 – August 2018, e) July 2019 – February 2019, f) January*
 413 *2021 – July 2019, g) June 2022 – January 2021. In each case, the colormap of elevation differences is overlapping the most*
 414 *recent DEM: b) November 2017, c) August 2018, d) February 2019, e) July 2019, f) January 2021 and g) June 2022. The red*
 415 *line corresponds to the N-S profiles presented in figure 6a.*

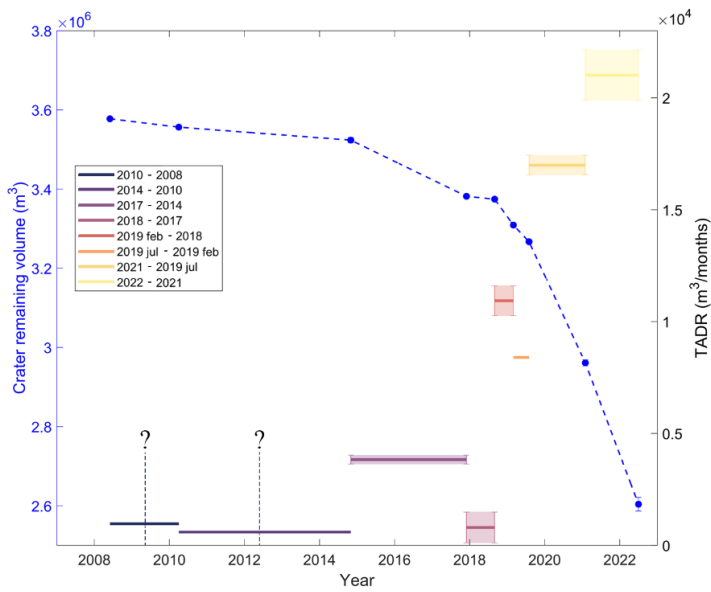
a)



b)



c)

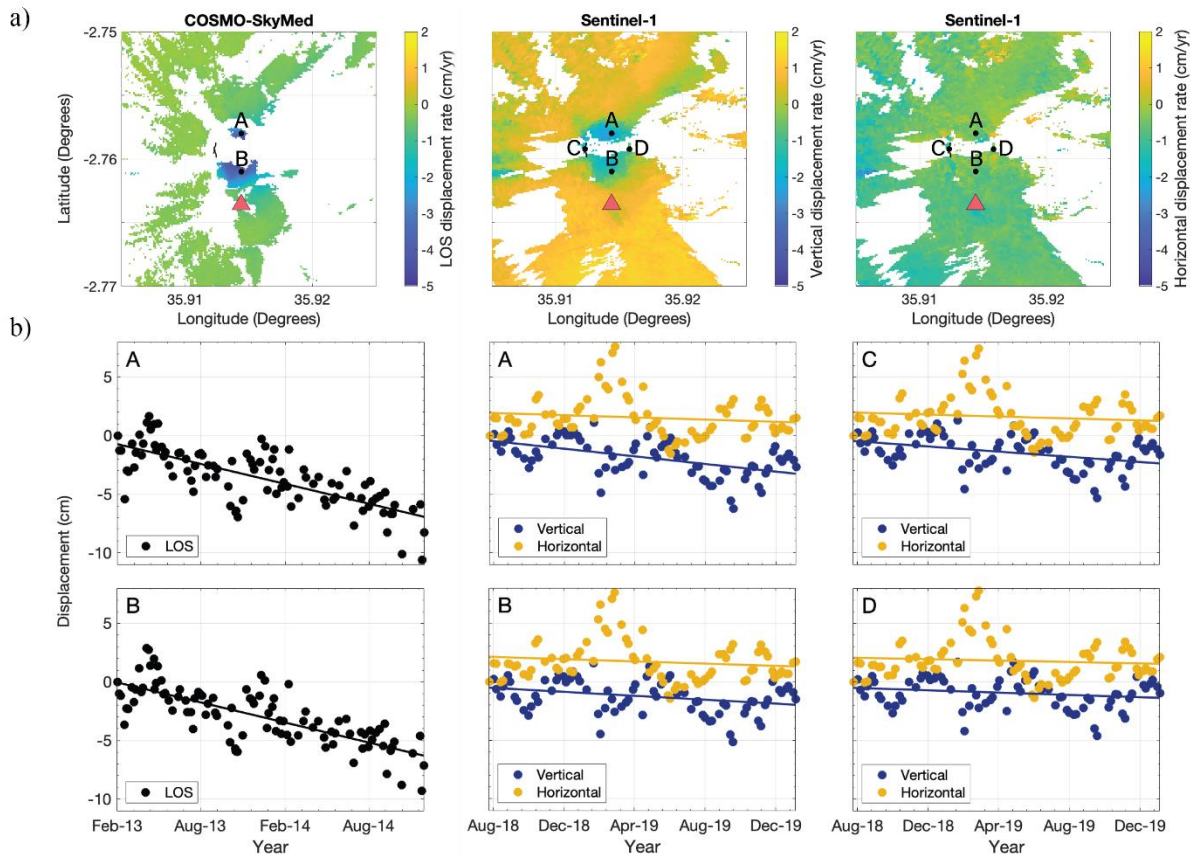


416

417 Figure 6: a) N-S profile of each reconstructed DEM (Profile drawn on figure 5a). Purple dashed line represents the base level
 418 used to fill in the October 2014 missing data. Blue and dark blue dashed lines represent the assumed shapes used to estimate
 419 the 2010 and 2008 crater volumes, respectively. B) Crater depth evolution over time. Dark blue and blue colors correspond to

420 estimates performed by Chris Weber in 2008 and David Sherrod in 2010, respectively (Global Volcanism Program, 2008,
 421 2010). The error associated with these measurements is unknown and represented by the error bar with a question mark. C)
 422 Crater remaining volume (blue dashed line, blue axis) and emission rate (solid lines, black axis) evolution over time (shaded
 423 areas correspond to the error). Error bars associated to the crater volume estimate are displayed but in most cases are
 424 comprised within the size of the data point.

425



426

427 *Figure 7: a) Cumulative surface displacement maps from COSMO-SkyMed (February 2013 – November 2014) and Sentinel-1*
 428 *(July 2018 – January 2020) data and b) time-series plots for points A through D. The red triangle represents the Oldoinyo*
 429 *Lengai summit, and the black outline represents the observed fissure on the western cone flank. The InSAR time-series reference*
 430 *coordinates are -2.754°, 35.871°.*

431 4. Discussion

432 4.1. Morphological evolution and shallow plumbing system

433 Numerous morphological changes are observable over time within the crater formed by the 2007-08
 434 eruption at Oldoinyo Lengai. A new natrocarbonatite lava platform has developed, progressively
 435 covering the older formations and filling the crater (Figure 5). We show that, within this platform the
 436 location of the active centers migrates over time from the northern region of the crater towards the
 437 center. This observation suggests subsurface changes in the geometry of OL's shallow plumbing system
 438 feeding lava emission at the surface. This interpretation is supported by other morphological changes
 439 including the formation and destruction of pools and hornitos on the lava platform. It appears that the
 440 largest structures were localized in the north part of the crater prior to July 2019, after which, large-scale

441 structures developed solely within the center of the platform. This behavior indicates that the lava flux
442 has been progressively redirected towards the center of OL's crater and has remained stable in this area
443 since. This observation is confirmed by the data presented in Reiss et al., (2023) that show a thermal
444 signal localized in the central part of the crater during the year 2019. The observed vent alignment on
445 the DEMs also suggests an E-W oriented shallow feeding system. Interestingly, Kervyn et al., (2008)
446 made similar observations of vent alignments at OL but oriented in a N-S direction at that time. Kervyn
447 et al., (2008) also reported very shallow interconnected magma reservoirs directly below the collapsed
448 remnants of large hornitos structures, as observed in June 2022. We also observe an evolution in the
449 eruptive style at OL over time. Vent structures were low in elevation (<10 m) prior to January 2021.
450 This suggests an eruptive activity composed mostly of lava flows as it will tend to direct the flux in the
451 main slope direction and propagate over a long distance (several tens of meters). On the other end, our
452 data suggest that the more recent activity has been dominated by spattering that favor a radial short range
453 distribution of the erupted products, hence allowing the formation of higher structures.

454 These observations tend to indicate that an E-W feeding system has been created or reactivated in OL's
455 pit crater and that the magma flux has been migrating through this system and increasing over time. A
456 potential explanation for an E-W oriented feeding system is related to the morphology of OL summit
457 area. The 2008 cone rests on a relatively flat platform composed of natrocarbonatites formed north of
458 the summit over the last century (Klaudius and Keller, 2006). The southern part of the 2008 cone is
459 bounded by the topography of the volcano's summit which provides stability to the cone structure. On
460 the other hand, the northern part of the cone is directly built up on lava flows accumulated (Figure 2 in
461 Klaudius and Keller, 2006) on the northern edge of that flat platform overlying the steep outer flank
462 (Figure 1c, d and e). Furthermore, fumaroles are regularly observed on the upper flanks of the volcano,
463 especially close to the 100 m fissure on the west part of the 2008 cone and on the northern flanks, likely
464 generating an alteration of the natrocarbonatites in these areas. Such differences of stability between the
465 northern and southern parts of the 2008 cone could impact the stress field within the pit crater, favoring
466 N-S extension stress field that would favor an E-W oriented feeding system at shallow level.

467 The central part of the crater is one of two primary regions of localized eruptive activity in OL's crater.
468 An active vent on the western edge of the crater (V1) has been active since before October 2014. Figure
469 2e displays a view of the western side of the crater in March 2010. At that time the western hornito (V1)
470 was not formed but a small cone with a large vent at its summit is visible. This structure is most likely
471 one of the first stages of V1 formation. From November 2017 until at least February 2019, V1 stopped
472 emitting, before reactivating. Interestingly, the activity of the central lava field and the vent V1 appear
473 to be anti-correlated (Figure 5). During the 6 months period August 2018 – February 2019 when V1 was
474 in quiescence, the lava field volume increased by $\approx 8.4 \times 10^4 \text{ m}^3$, twice as much as during the 9 months
475 period November 2017 – August 2018. During the 5 months period February 2019 to July 2019 the lava
476 field volume only increased by $\approx 5.2 \times 10^4 \text{ m}^3$, when V1 was being reactivated. Thermal InfraRed satellite

477 data confirm V1 reactivation by showing an absence of thermal signal on the western part of OL's crater
478 between March and May 2019 and then the presence of a hotspot in June 2019 (Reiss et al., 2023). After
479 this, V1 appears to be quiescent again at least until March 2020 according to MSI-Sentinel 2 and OLI-
480 Landsat 8. However, we can observe that V1 increased again in volume in January 2021 and June 2022
481 indicating a new activation of the vent between March 2020 and January 2021. From July 2019, the lava
482 field volume steadily increased again until June 2022. It appears that lava emission at the western vents
483 ceased while the central vents were migrating from the northern part to the central region of the crater
484 from November 2017 to February 2019. From February 2019 onwards, both areas were active
485 simultaneously. After the merging of all central vents into one main hornito (V17) in January 2021,
486 OL's crater displayed only two main active vents, the central (V17) and western (V1) vents (Figure 5f).
487 In June 2022, we show that the number of vents increased again and spread along an E-W axis between
488 the central and west active areas. We explain this observation by considering that the collapse of V1 and
489 V17's summits likely clogged their main conduits. The result of this is a stress distribution change within
490 the hornitos plumbing systems, consequently forcing lateral magma migration and the formation of new
491 vents in the vicinity of V1 and V17 (Figure 5g).

492 Temporal vent migration, successive vent activation and deactivation as well as simultaneous emission
493 from multiple vents is well known and regularly observed at other open vent volcanoes, including
494 Stromboli in Italy and Yasur in Vanuatu (Nabyl et al., 1997; Oppenheimer et al., 2006; Harris and
495 Ripepe, 2007; Gaudin et al., 2014, 2017; Simons et al., 2020). This phenomenon is often explained by
496 interconnected conduits and shallow reservoirs typically no more than a few hundred meters deep, *e.g.*,
497 ≈ 300 m depth in the case of Stromboli volcano (Harris and Ripepe, 2007). Despite further geophysical
498 constraints on OL's deep plumbing system (Reiss et al., 2022), substantial knowledge gaps remain
499 regarding its shallow plumbing system. It has been suggested in Kervyn et al., (2008) that vent
500 migrations at OL were related to extremely shallow magma reservoirs (*i.e.*, few tens of meters depth).
501 The observed shifts in active area within OL's crater suggest regular reconfiguration of the shallow
502 plumbing system associated to the formation and clogging of preferential eruption pathways between
503 magma storage and surface. Thermal erosion is also a phenomenon observed at OL that could play a
504 significant role in the motion of active vents (Dawson et al., 1990; Kervyn et al., 2008). It also appears
505 that higher hornitos, associated with spattering, form when less vents are active. It could be explained
506 by the flow being concentrated on fewer vents, hence, building a higher pressure.

507 The overall TADR at OL exhibits a steady increase since August 2018, culminating at 2.1×10^4 m³/month
508 (8×10^{-3} m³/s) in June 2022. Over the past 4 years, the TADR was 7 times greater than the average value
509 obtained for the steady period 2010-2018 (10^{-3} m³/s), in good agreement with previously documented
510 emission rates of 2×10^{-3} m³/s reported by Dawson et al., (1990). A distinct change in the TADR has
511 occurred during the studied period, with a stable, low rate in the period 2010-2018 and an increasing
512 rate in the period 2018-2022. Thus, it appears that somewhere between August 2018 and February 2019,

513 OL volcano experienced a change in its magma feeding system that modified both the lava flux and the
514 conduit geometry. This is a crucial finding with a direct implication on the remaining time before a new
515 overflow event may initiate.

516 **4.2. Instabilities**

517 At least 4 major crater wall collapses took place during the studied period, 2 during the period October
518 2014 – November 2017, 1 between August 2018 and February 2019 and 1 between July 2019 and
519 January 2021. The presence of meter-size blocks accumulated on the crater floor in these areas confirms
520 the occurrence of these events. Collapses appear restricted to the SW crater wall and we explain this in
521 the context of the crater geometry. The observed collapses affect the sub-vertical walls of the lower part
522 of the crater. While most of the steep-sided walls of the crater are vertical, in the SW region, the crater
523 walls are overhanging with an angle of $\approx 70^\circ$ to the horizontal. These overhanging crater walls are
524 therefore less stable than the rest of the lower crater section. Based on images taken during and after the
525 2007-08 paroxysm we can see that the newly formed crater experienced multiple collapses (Figure 2).
526 These collapses appear to have taken place mostly in the eastern and northern sections of the crater,
527 some of which impacted the crater up to its upper section. Based on our data we know that these
528 collapses occurred between July 2008 and February 2009. Interestingly, climbers reported hearing
529 “strong thundering noises” and sensed tremors on 12 October 2008, while being close to the summit
530 (Global Volcanism Program, 2009). Thick steam from the crater was also reported on 26 October 2008.
531 These two events could be related to the aforementioned collapses. The northern and eastern pit crater
532 walls have remained stable since. However, in the case of the SW overhanging walls, it took many years
533 to collapse. One possible explanation could be that the activity migration from the north to the center of
534 the crater over the years, together with the increase in TADR, have generated new instabilities within
535 OL crater through shaking and fracturing.

536 An additional sign of instability is noted on the outer part of the cone formed in 2008, where a 100 m
537 long-fissure formed on the western flank very close to the contact between the newly formed cone and
538 previous deposits (Figure 1e). Based on our dataset and previous studies, we can confirm that this fissure
539 dates back to at least 2013 (Global Volcanism Program, 2013b). This feature presents a future potential
540 hazard. Should this fissure weakens the integrity of the cone, the flanks could ultimately fail and generate
541 collapse within the pit crater. This would be a significant hazard for any climbers on the edifice at that
542 time. No clear evolution of the fissure is observable over the years in our data but observations on the
543 field suggest that the fissure is getting larger. Based on our DEM comparison, the overall crater flanks
544 and inner walls do not show any motion that could be related to it. However, the InSAR data clearly
545 indicate a subsidence of the 2008 cone area (Figure 7). This subsidence appears to be of larger magnitude
546 during the February 2013 – November 2014 period with a displacement of ≈ -3.4 cm/year compared to
547 the period July 2018 – January 2020 with a vertical displacement between -0.6 and -2.0 cm/year. The

548 observed surface displacement is most certainly a gravitational subsidence that can potentially be
549 associated with a ring fault system as observed at Sierra Negra (Amelung et al., 2000; Jónsson et al.,
550 2005; Jónsson, 2009), Tendürek (Bathke et al., 2013) and Okmok (Johnson et al., 2010) volcanoes. The
551 decrease of subsidence rate between the periods February 2013 – August 2014 and August 2018 –
552 December 2019 could be partially related to the increase of filling rate observed since 2018 that is
553 limiting inward dipping movement by stabilizing the inner crater wall. Furthermore, the western flank
554 fissure could result from this subsidence and is likely accommodating some of it. The fissure could
555 indeed be related to a destabilization of the young cone towards the pit crater. Considering that the SW
556 walls of the lower crater section display a 70° inclination to the horizontal and that the 100 m fissure on
557 the outer part of the cone covers the west area, we could assume that these two features are related.
558 These features could be part of a slow destabilization of the western flank of the cone towards the pit
559 crater. No motion of the western flank towards the crater's center is observed with the DEM comparison
560 which could be explained if the said motion is very slow (< 2-3 cm/month).

561 **4.3. Historical behavior and future implications**

562 Phases of effusive natrocarbonatite emissions refilling progressively OL's crater, as observed over the
563 past decade, have been described repeatedly in the recent history of this volcano. The 1917, 1966 and
564 2007 paroxysmal eruptions were all preceded by several years of effusive activity confined to the crater
565 (Dawson et al., 1968; Nyamweru, 1990; Dawson et al., 1995; Kervyn et al., 2010). Progressive filling
566 of the crater led to lava overflows and, ultimately, to the lava platform being removed by violent
567 explosive activity. During these effusive phases, the formation and destruction of large hornitos (or
568 needles) have also been reported, for example in 1910, a 40 to 50 m tall hornito located on the northern
569 rim of the crater (Dawson et al., 1995) and in 2006, a 60 m tall hornito located at the northwest overflow
570 (Global Volcanism Program, 2006). Migration in the location of active vents and the opening of new
571 vents have been described extensively at OL (*e.g.*, Dawson et al., 1994; Global Volcanism Program,
572 2013a). The TADRs calculated in this study are of similar magnitude to literature values from other
573 periods (Dawson et al., 1990). A marked difference between the 2007-08 paroxysm compared to
574 previous ones is the absence of a subsequent hiatus in OL's activity. The 1917, 1940 and 1966
575 paroxysmal events were followed by a quiescent period that, in some cases, lasted several years (Dawson
576 et al., 1995; Kervyn et al., 2010). It is however important to remain careful with this information as the
577 number of observations historically may not have been as numerous as in recent years and the lack of
578 observational tools (*e.g.*, thermal cameras, satellite, UAS) may have limited the detection of activity and
579 contributed to an observational bias.

580 If the 2022 emission rate (Table 3) is sustained in the coming years, the crater lower section could be
581 filled within 5 years allowing again climbers to go down in OL's crater. About 8.7 years would be
582 required for the crater floor to reach once again the crater rim's lowest elevation point (2887 m in the

583 W-NW area) and to have natrocarbonatite overflow the crater onto the outer flanks. However, assuming
584 an increasing emission rate following the same trend it has since 2018, the crater could be filled in as
585 little as 6 years.

586 In terms of hazard implications, further collapses at the level of the lower crater section are to be
587 expected in the coming years, especially in the SW area, until the lower section is filled with lava.
588 Indeed, the overhanging walls of this crater section are likely to be still unstable. Once the lower section
589 has been filled and the lava level approaches the crater rim, hazards for climbers will include hornitos
590 and crater floor collapses as well as small-scale explosions and lava flows. Comprehensive management
591 plans and scenario-based risk assessments will be required to safely manage volcano tourism. Lava
592 overflows may resume at OL once the lava platform reaches the crater rim level, as previously reported
593 prior to the 1917 and 2007 paroxysms. These overflows will most likely take place in the W-NW area
594 of the crater where the rim elevation is lowest. As this is the area where the current climbing path is
595 reaching the crater rim, any lava overflow could potentially disturb or prevent reaching the summit with
596 the current path. Finally, the 2008 cone stability should be monitored in the future as we observed a
597 subsidence of the whole structure over the years and the presence of a fissure on the western flank. It is
598 important to follow this evolution in the coming years to anticipate potential destabilization of the cone
599 leading to flank collapses.

600 Although data collected as part of this study do not allow us to get insights into when OL volcano may
601 experience a new paroxysm, based on the knowledge gained from past events, the time span between
602 two paroxysms varies from 9 to 40 years. With only 15 years having elapsed since the last paroxysm,
603 OL is therefore still towards the lower end of inter-eruption period duration. It is also important to
604 highlight that even the maximum TADR of $2.1 \times 10^4 \text{ m}^3/\text{month}$ remains an order of magnitude lower with
605 respect to the estimate of $2 \times 10^5 \text{ m}^3/\text{month}$ obtained for August 2007, just prior to the 2007-08 paroxysm
606 (Kervyn et al., 2010). Despite this, the recent dynamic evolution of OL's shallow plumbing system and
607 the abrupt increase in emission rate emphasize the need to monitor this volcano closely and regularly –
608 even through simple photographic techniques.

609 **4.4. The potential in crowd-sourced data**

610 In this study, we evidence the potential that resides in videos and pictures captured by volcanologists,
611 locals and tourists, to not only document visual changes in activity but also to reconstruct quantitatively
612 the morphological evolution of a remote volcanic crater where in situ monitoring is challenging and
613 therefore limited. This study also highlights the value of open collaboration between scientists from
614 different fields, allowing this study to benefit from other researchers' field work by getting access to
615 data acquired for other purposes than photogrammetry.

616 The use of crowd-sourced data is becoming increasingly common and has recently enabled the
617 reconstruction of the chronology of the 2013 eruption of San Miguel volcano, El Salvador (Brown et

618 al., 2022). The addition of crowd-sourced data revealed phenomena that would not have been detected
619 based on analysis of the deposits alone (Brown et al., 2022). Technological development over the past
620 two decades has provided most individuals with miniaturized cameras (phones, compact cameras) and
621 this becomes a crucial data source for scientists, especially at remote and unmonitored volcanoes such
622 as in East Africa (Fontijn et al., 2018; Biggs et al., 2021). The drawback of such data is the added
623 complexity of pre-processing and integration. These data are not acquired under the same conditions
624 (point of view, lighting conditions, number of images, camera type), have different properties, and thus
625 can be challenging to compile in a coherent dataset for photogrammetric analysis and comparison. For
626 example, several retrieved datasets in this study were inadequate and we were unable to reconstruct
627 DEMs at sufficiently high resolution (2008, 2010 and 2012). Another, DEM turned out incomplete, *i.e.*,
628 the 2014 DEM. However, in most cases it was possible to produce high-resolution DEMs accurately co-
629 registered. Although the data were from various origins, robust quantitative assessments of crater depth,
630 lava surface areas and emission rates were performed, providing a unique insight into the activity of OL
631 over the years.

632 To further improve the results of future studies based on crowd-sourced data some straightforward and
633 practical guidelines could be provided for locals and tourists willing to collect and share data during
634 visits to remote volcanoes. The photogrammetric technique used in this study requires to follow only 4
635 basic principles. First, a minimum number of pictures is necessary depending on the size of the area of
636 interest (in our case 80 pictures was the lower limit). Second, the pictures need to be taken from as many
637 different viewing geometries as possible. Third, pictures need to partially overlap to facilitate the SfM-
638 MVS processing. Fourth, the pictures need to be taken during even lighting conditions, ideally around
639 midday to avoid shadows. Finally, for people remaining over several days, acquiring the data in the
640 same conditions every day would facilitate comparisons.

641 **5. Conclusion**

642 Using crowd-sourced image data acquired at OL and analyzing these datasets with SfM-MVS, we have
643 reconstructed 7 DEMs of the pit crater to evaluate its spatial and temporal morphological changes
644 occurring since the 2007-08 paroxysm. Many instabilities in OL's crater are highlighted in this study,
645 including crater walls and hornitos collapses as well as the presence of a 100 m long fracture on the
646 western outer cone flank. Our results document several fundamental changes in the shallow plumbing
647 system, including vent migration and a succession of active and quiet phases. We observe that OL's
648 active vents have migrated from the northern crater area towards its center, while the southern area never
649 displayed any activity. The vents have merged into tall hornitos before again scattering after the hornitos
650 collapses suggesting significant changes in the stress field over time. We also observe an E-W vent
651 alignment since 2019 combined with the formation of taller and larger hornitos suggesting an increase
652 in spattering in OL eruptive style. The refill rate of the pit crater displays a permanent increase over

653 time, with a distinct acceleration occurring since 2018 and culminating at a maximum rate of 2.1×10^4
654 m^3/months in 2022. Assuming a similar emission rate is maintained in the coming years, the crater could
655 be filled entirely and start to again overflow within 8 years. Regular monitoring of the OL pit crater is
656 therefore critical to accurately forecast its future evolution in order to mitigate the risk to nearby
657 populations and tourists.

658 By combining pictures taken by tourists and scientists we were able to generate an unprecedented dataset
659 spanning the past 8 years of activity at OL volcano. Further, this study confirmed that, when used
660 correctly, crowd-sourced images represent an extensive and cost-effective source of data for scientists
661 that could provide invaluable qualitative and quantitative constraints on activity at volcanoes that are
662 not permanently monitored, such as OL. With respect to the SfM-MVS methodology, only a few criteria
663 (pertaining to the number of images, viewing geometries, overlap and lighting conditions) must be
664 respected to acquire useful data in the form of high-quality images. Consequently, if such information
665 is passed on to travel agencies and local populations, this presents a collaborative opportunity to involve
666 both community members and tourists in the acquisition and sharing of scientific data whilst at the same
667 time promoting a forum for effective and sustained two-way knowledge exchange.

668 **6. Acknowledgement**

669 The authors want to thank the contribution of Sylvain Chermette from 80 jours voyages and the Société
670 de Volcanologie de Genève (SVG), who provided data for June 2022. We also want to thank Michael
671 Dalton-Smith and Gian Schachenmann from Serengeti Films and Kicheche Natural History Unit, for
672 providing us data for January 2021. We want to thank Patrick Marcel, Regis Etienne and Marc Caillet
673 from the SVG for providing data covering August 2018 and February 2019. Finally, the authors want to
674 thank Benoit Wilhelmi, Ben Beeckmans, David Sherrod and Franck Mockel for providing pictures of
675 OL crater for 2008, 2009, 2010 and 2012, respectively. PYT acknowledges the support of the Research
676 Foundation Flanders (FWO), through the MORPHEUS postdoc project (grant FWOTM996). BS was
677 supported by the GuiDANCE project (Belgian Science Policy Office, FED-tWIN Programme, Grant
678 Prf-2019-066). KL and EJM acknowledge funding for the July 2019 expedition through the Alfred P.
679 Sloan Foundation's support of the Deep Carbon Observatory Deep Earth Carbon Degassing program
680 (DECADE). CW and CH acknowledge the support from the National Science Foundation (NSF)
681 CAREER EAR 1945417 and EAR 1923943. We also thank the Tanzania Commission for Science and
682 Technology (COSTECH) for field permits and all the guides and porters for their help during field work.
683 LF & GC acknowledge the support of the French National Research Agency through the national
684 program "Investissements d'avenir" with the reference ANR-10-LABX-21-01/LABEX
685 RESSOURCES21, and through the project GECO-REE (ANR-16-CE01-0003-01). This is CRPG
686 contribution number **xxxx** and GECO-REE contribution number **x**.

687

688 **7. Data Availability**

689 All the data mentioned in this article are available upon request to the first author.

690

691 **8. Reference**

692 Amelung, F., Jónsson, S., Zebker, H., and Segall, P., 2000, Widespread uplift and ‘trapdoor’ faulting on
693 Galápagos volcanoes observed with radar interferometry: *Nature*, v. 407, p. 993–996,
694 doi:10.1038/35039604.

695 Barrière, J. et al., 2022, Intra-Crater Eruption Dynamics at Nyiragongo (D.R. Congo), 2002–2021:
696 *Journal of Geophysical Research: Solid Earth*, v. 127, p. e2021JB023858,
697 doi:10.1029/2021JB023858.

698 Bathke, H., Sudhaus, H., Holohan, E. p., Walter, T.R., and Shirzaei, M., 2013, An active ring fault
699 detected at Tendürek volcano by using InSAR: *Journal of Geophysical Research: Solid Earth*,
700 v. 118, p. 4488–4502, doi:10.1002/jgrb.50305.

701 Biggs, J., Ayele, A., Fischer, T.P., Fontijn, K., Hutchison, W., Kazimoto, E., Whaler, K., and Wright,
702 T.J., 2021, Volcanic activity and hazard in the East African Rift Zone: *Nature Communications*,
703 v. 12, p. 6881, doi:10.1038/s41467-021-27166-y.

704 Blewitt, G., Hammond, W., and Kreemer, C., 2018, Harnessing the GPS Data Explosion for
705 Interdisciplinary Science: *Eos*, v. 99, doi:10.1029/2018eo104623.

706 Bosshard-Stadlin, S.A., Mattsson, H.B., and Keller, J., 2014, Magma mixing and forced exsolution of
707 CO₂ during the explosive 2007–2008 eruption of Oldoinyo Lengai (Tanzania): *Journal of*
708 *Volcanology and Geothermal Research*, v. 285, p. 229–246,
709 doi:10.1016/j.jvolgeores.2014.08.017.

710 Brown, R.J., Hernández, W., Escobar, D., Gutierrez, E., Crummy, J., Cole, R., and Tournigand, P.-Y.,
711 2022, Reconstruction of the 29th December 2013 eruption of San Miguel volcano, El Salvador,
712 using video, photographs, and pyroclastic deposits: *Volcanica*, v. 5, p. 271–293,
713 doi:10.30909/vol.05.02.271293.

714 Carr, B.B., Lev, E., Vanderkluyesen, L., Moyer, D., Marliyani, G.I., and Clarke, A.B., 2022, The Stability
715 and Collapse of Lava Domes: Insight From Photogrammetry and Slope Stability Models
716 Applied to Sinabung Volcano (Indonesia): *Frontiers in Earth Science*, v. 10,
717 <https://www.frontiersin.org/articles/10.3389/feart.2022.813813> (accessed April 2023).

718 Civico, R. et al., 2021, Unoccupied Aircraft Systems (UASs) Reveal the Morphological Changes at
719 Stromboli Volcano (Italy) before, between, and after the 3 July and 28 August 2019 Paroxysmal
720 Eruptions: *Remote Sensing*, v. 13, p. 2870, doi:10.3390/rs13152870.

721 Darmawan, H., Walter, T.R., Troll, V.R., and Budi-Santoso, A., 2018, Structural weakening of the
722 Merapi dome identified by drone photogrammetry after the 2010 eruption: *Natural Hazards and*
723 *Earth System Sciences*, v. 18, p. 3267–3281, doi:10.5194/nhess-18-3267-2018.

724 Dawson, J.B., Bowden, P., and Clark, G.C., 1968, Activity of the carbonatite volcano Oldoinyo Lengai,
725 1966: *Geologische Rundschau*, v. 57, p. 865–879, doi:10.1007/BF01845369.

726 Dawson, J.B., Keller, J., and Nyamweru, C., 1995, Historic and Recent Eruptive Activity of Oldoinyo
727 Lengai, in Bell, K. and Keller, J. eds., *Carbonatite Volcanism: Oldoinyo Lengai and the*

- 728 Petrogenesis of Natrocarbonatites, Berlin, Heidelberg, Springer, IAVCEI Proceedings in
729 Volcanology, p. 4–22, doi:10.1007/978-3-642-79182-6_2.
- 730 Dawson, J.B., Pinkerton, H., Norton, G.E., and Pyle, D.M., 1990, Physicochemical properties of alkali
731 carbonatite lavas: Data from the 1988 eruption of Oldoinyo Lengai, Tanzania: *Geology*, v. 18,
732 p. 260–263, doi:10.1130/0091-7613(1990)018<0260:PPOACL>2.3.CO;2.
- 733 Dawson, J.B., Pinkerton, H., Pyle, D.M., and Nyamweru, C., 1994, June 1993 eruption of Oldoinyo
734 Lengai, Tanzania: Exceptionally viscous and large carbonatite lava flows and evidence for
735 coexisting silicate and carbonate magmas: *Geology*, v. 22, p. 799–802, doi:10.1130/0091-
736 7613(1994)022<0799:JEOOLT>2.3.CO;2.
- 737 Delhaye, L., and Smets, B., 2021, Time-Series in Structure-from-Motion Photogrammetry: Testing Co-
738 Registration Approaches for Topographic Change Analysis, in 2021 IEEE International
739 Geoscience and Remote Sensing Symposium IGARSS, p. 4648–4651,
740 doi:10.1109/IGARSS47720.2021.9553796.
- 741 Dering, G.M., Micklethwaite, S., Thiele, S.T., Vollgger, S.A., and Cruden, A.R., 2019, Review of
742 drones, photogrammetry and emerging sensor technology for the study of dykes: Best practises
743 and future potential: *Journal of Volcanology and Geothermal Research*, v. 373, p. 148–166,
744 doi:10.1016/j.jvolgeores.2019.01.018.
- 745 Derrien, A., Villeneuve, N., Peltier, A., Beauducel, F., 2015. Retrieving 65 years of volcano summit
746 deformation from multitemporal structure from motion: The case of Piton de la Fournaise (La
747 Réunion Island). *Geophys. Res. Lett.* 42, 6959–6966. <https://doi.org/10.1002/2015GL064820>.
- 748 Dille, A., Kervyn, F., Handwerker, A.L., d'Oreye, N., Derauw, D., Mugaruka Bibentyo, T., Samsonov,
749 S., Malet, J.-P., Kervyn, M., and Dewitte, O., 2021, When image correlation is needed:
750 Unravelling the complex dynamics of a slow-moving landslide in the tropics with dense radar
751 and optical time series: *Remote Sensing of Environment*, v. 258, p. 112402,
752 doi:10.1016/j.rse.2021.112402.
- 753 Feurer, D., and Vinatier, F., 2018, Joining multi-epoch archival aerial images in a single SfM block
754 allows 3-D change detection with almost exclusively image information: *ISPRS Journal of*
755 *Photogrammetry and Remote Sensing*, v. 146, p. 495–506, doi:10.1016/j.isprsjprs.2018.10.016.
- 756 Fonstad, M.A., Dietrich, J.T., Courville, B.C., Jensen, J.L., and Carbonneau, P.E., 2013, Topographic
757 structure from motion: a new development in photogrammetric measurement: *Earth Surface*
758 *Processes and Landforms*, v. 38, p. 421–430, doi:10.1002/esp.3366.
- 759 Fontijn, K., McNamara, K., Zafu Tadesse, A., Pyle, D.M., Dessalegn, F., Hutchison, W., Mather, T.A.,
760 and Yirgu, G., 2018, Contrasting styles of post-caldera volcanism along the Main Ethiopian
761 Rift: Implications for contemporary volcanic hazards: *Journal of Volcanology and Geothermal*
762 *Research*, v. 356, p. 90–113, doi:10.1016/j.jvolgeores.2018.02.001.
- 763 France, L., Brouillet, F., and Lang, S., 2021, Early carbonatite magmatism at Oldoinyo Lengai volcano
764 (Tanzania): carbonatite–silicate melt immiscibility in Lengai I melt inclusions: *Comptes*
765 *Rendus. Géoscience*, v. 353, p. 273–288, doi:10.5802/crgeos.99.
- 766 Gaudin, D., Taddeucci, J., Scarlato, P., Harris, A., Bombrun, M., Del Bello, E., and Ricci, T., 2017,
767 Characteristics of puffing activity revealed by ground-based, thermal infrared imaging: the
768 example of Stromboli Volcano (Italy): *Bulletin of Volcanology*, v. 79, p. 24,
769 doi:10.1007/s00445-017-1108-x.

- 770 Gaudin, D., Taddeucci, J., Scarlato, P., Moroni, M., Freda, C., Gaeta, M., and Palladino, D.M., 2014,
771 Pyroclast Tracking Velocimetry illuminates bomb ejection and explosion dynamics at
772 Stromboli (Italy) and Yasur (Vanuatu) volcanoes: *Journal of Geophysical Research: Solid*
773 *Earth*, v. 119, p. 2014JB011096, doi:10.1002/2014JB011096.
- 774 Girardeau-Montaut, D., 2016, CloudCompare., <https://www.danielgm.net/cc>.
- 775 Global Volcanism Program, 2013a, Ol Doinyo Lengai (222120) in *Volcanoes of the World*, v. 4.11.0
776 (08 Jun 2022). Venzke, E (ed.). Smithsonian Institution. Downloaded 14 Jun 2022
777 (<https://volcano.si.edu/volcano.cfm?vn=222120>). [https://doi.org/10.5479/si.GVP.VOTW4-](https://doi.org/10.5479/si.GVP.VOTW4-2013)
778 2013:
- 779 Global Volcanism Program, 2018, Report on Ol Doinyo Lengai (Tanzania) (Krippner, J.B., and Venzke,
780 E., eds.). *Bulletin of the Global Volcanism Network*, 43:10. Smithsonian Institution.
781 <https://doi.org/10.5479/si.GVP.BGVN201810-222120>:
- 782 Global Volcanism Program, 2006, Report on Ol Doinyo Lengai (Tanzania) (Wunderman, R., ed.).
783 *Bulletin of the Global Volcanism Network*, 31:3. Smithsonian Institution.
784 <https://doi.org/10.5479/si.GVP.BGVN200603-222120>:
- 785 Global Volcanism Program, 2008, Report on Ol Doinyo Lengai (Tanzania) (Wunderman, R., ed.).
786 *Bulletin of the Global Volcanism Network*, 33:6. Smithsonian Institution.
787 <https://doi.org/10.5479/si.GVP.BGVN200806-222120>:
- 788 Global Volcanism Program, 2009, Report on Ol Doinyo Lengai (Tanzania) (Wunderman, R., ed.).
789 *Bulletin of the Global Volcanism Network*, 34:2. Smithsonian Institution.
790 <https://doi.org/10.5479/si.GVP.BGVN200902-222120>:
- 791 Global Volcanism Program, 2010, Report on Ol Doinyo Lengai (Tanzania) (Wunderman, R., ed.).
792 *Bulletin of the Global Volcanism Network*, 35:5. Smithsonian Institution.
793 <https://doi.org/10.5479/si.GVP.BGVN201005-222120>:
- 794 Global Volcanism Program, 2013b, Report on Ol Doinyo Lengai (Tanzania) (Wunderman, R., ed.).
795 *Bulletin of the Global Volcanism Network*, 38:6. Smithsonian Institution.
796 <https://doi.org/10.5479/si.GVP.BGVN201306-222120>:
- 797 Gonzalez-Santana, J., Wauthier, C., and Burns, M., 2022, Links between volcanic activity and flank
798 creep behavior at Pacaya Volcano, Guatemala: *Bulletin of Volcanology*, v. 84, p. 84,
799 doi:10.1007/s00445-022-01592-2.
- 800 Hanagan, C., La Femina, P.C., Rodgers, M., 2020. Changes in Crater Morphology Associated With
801 Volcanic Activity at Telica Volcano, Nicaragua. *Geochem. Geophys. Geosystems* 21,
802 e2019GC008889. <https://doi.org/10.1029/2019GC008889>.
- 803 Harris, A., Dehn, J., Calvari, S., 2007. Lava effusion rate definition and measurement: a review. *Bull.*
804 *Volcanol.* 70, 1–22. <https://doi.org/10.1007/s00445-007-0120-y>. Harris, A., and Ripepe, M.,
805 2007, Synergy of multiple geophysical approaches to unravel explosive eruption conduit and
806 source dynamics – A case study from Stromboli: *Chemie der Erde - Geochemistry*, v. 67, p. 1–
807 35, doi:10.1016/j.chemer.2007.01.003.
- 808 Hendrickx, H., De Sloover, L., Stal, C., Delaloye, R., Nyssen, J., and Frankl, A., 2020, Talus slope
809 geomorphology investigated at multiple time scales from high-resolution topographic surveys
810 and historical aerial photographs (Sanetsch Pass, Switzerland): *Earth Surface Processes and*
811 *Landforms*, v. 45, p. 3653–3669, doi:10.1002/esp.4989.

- 812 Höhle, J., Höhle, M., 2009. Accuracy assessment of digital elevation models by means of robust
813 statistical methods. *ISPRS J. Photogramm. Remote Sens.* 64, 398–406.
814 <https://doi.org/10.1016/j.isprsjprs.2009.02.003>.
- 815 James, M.R., and Robson, S., 2014, Sequential digital elevation models of active lava flows from
816 ground-based stereo time-lapse imagery: *ISPRS Journal of Photogrammetry and Remote*
817 *Sensing*, v. 97, p. 160–170, doi:10.1016/j.isprsjprs.2014.08.011.
- 818 James, M.R., and Robson, S., 2012, Straightforward reconstruction of 3D surfaces and topography with
819 a camera: Accuracy and geoscience application: *Journal of Geophysical Research: Earth*
820 *Surface*, v. 117, doi:<https://doi.org/10.1029/2011JF002289>.
- 821 James, M.R., Robson, S., d'Oleire-Oltmanns, S., and Niethammer, U., 2017, Optimising UAV
822 topographic surveys processed with structure-from-motion: Ground control quality, quantity
823 and bundle adjustment: *Geomorphology*, v. 280, p. 51–66,
824 doi:10.1016/j.geomorph.2016.11.021.
- 825 James, M.R., and Varley, N., 2012, Identification of structural controls in an active lava dome with high
826 resolution DEMs: Volcán de Colima, Mexico: *Geophysical Research Letters*, v. 39,
827 doi:10.1029/2012GL054245.
- 828 Javernick, L., Hicks, D.M., Measures, R., Caruso, B., and Brasington, J., 2016, Numerical Modelling of
829 Braided Rivers with Structure-from-Motion-Derived Terrain Models: *River Research and*
830 *Applications*, v. 32, p. 1071–1081, doi:10.1002/rra.2918.
- 831 Johnson, J.H., Prejean, S., Savage, M.K., and Townend, J., 2010, Anisotropy, repeating earthquakes,
832 and seismicity associated with the 2008 eruption of Okmok volcano, Alaska: *Journal of*
833 *Geophysical Research: Solid Earth*, v. 115, doi:10.1029/2009JB006991.
- 834 Jónsson, S., 2009, Stress interaction between magma accumulation and trapdoor faulting on Sierra
835 Negra volcano, Galápagos: *Tectonophysics*, v. 471, p. 36–44, doi:10.1016/j.tecto.2008.08.005.
- 836 Jónsson, S., Zebker, H., and Amelung, F., 2005, On trapdoor faulting at Sierra Negra volcano,
837 Galápagos: *Journal of Volcanology and Geothermal Research*, v. 144, p. 59–71,
838 doi:10.1016/j.jvolgeores.2004.11.029.
- 839 Keller, J., Klaudius, J., Kervyn, M., Ernst, G.G.J., and Mattsson, H.B., 2010, Fundamental changes in
840 the activity of the natrocarbonatite volcano Oldoinyo Lengai, Tanzania: *Bulletin of*
841 *Volcanology*, v. 72, p. 893–912, doi:10.1007/s00445-010-0371-x.
- 842 Kervyn, M., Ernst, G.G.J., Keller, J., Vaughan, R.G., Klaudius, J., Pradal, E., Belton, F., Mattsson, H.B.,
843 Mbede, E., and Jacobs, P., 2010, Fundamental changes in the activity of the natrocarbonatite
844 volcano Oldoinyo Lengai, Tanzania: *Bulletin of Volcanology*, v. 72, p. 913–931,
845 doi:10.1007/s00445-010-0360-0.
- 846 Kervyn, M., Ernst, G.G.J., Klaudius, J., Keller, J., Kervyn, F., Mattsson, H.B., Belton, F., Mbede, E.,
847 and Jacobs, P., 2008, Voluminous lava flows at Oldoinyo Lengai in 2006: chronology of events
848 and insights into the shallow magmatic system: *Bulletin of Volcanology*, v. 70, p. 1069–1086,
849 doi:10.1007/s00445-007-0190-x.
- 850 Klaudius, J., Keller, J., 2006. Peralkaline silicate lavas at Oldoinyo Lengai, Tanzania. *Lithos, Peralkaline*
851 *Rocks* 91, 173–190. <https://doi.org/10.1016/j.lithos.2006.03.017>.
- 852 Krieger, G., Moreira, A., Fiedler, H., Hajnsek, I., Werner, M., Younis, M., and Zink, M., 2007,
853 TanDEM-X: A Satellite Formation for High-Resolution SAR Interferometry: *IEEE*

- 854 Transactions on Geoscience and Remote Sensing, v. 45, p. 3317–3341,
855 doi:10.1109/TGRS.2007.900693.
- 856 Lague, D., Brodu, N., and Leroux, J., 2013, Accurate 3D comparison of complex topography with
857 terrestrial laser scanner: Application to the Rangitikei canyon (N-Z): ISPRS Journal of
858 Photogrammetry and Remote Sensing, v. 82, p. 10–26, doi:10.1016/j.isprsjprs.2013.04.009.
- 859 Laxton, K., 2020, Collection of lava samples from Ol Doinyo Lengai: Nature Reviews Earth &
860 Environment, v. 1, p. 438–438, doi:10.1038/s43017-020-0089-z.
- 861 Lucieer, A., Jong, S.M. de, and Turner, D., 2014, Mapping landslide displacements using Structure from
862 Motion (SfM) and image correlation of multi-temporal UAV photography: Progress in Physical
863 Geography: Earth and Environment, v. 38, p. 97–116, doi:10.1177/0309133313515293.
- 864 Mollex, G., Füre, E., Burnard, P., Zimmermann, L., Chazot, G., Kazimoto, E.O., Marty, B., and France,
865 L., 2018, Tracing helium isotope compositions from mantle source to fumaroles at Oldoinyo
866 Lengai volcano, Tanzania: Chemical Geology, v. 480, p. 66–74,
867 doi:10.1016/j.chemgeo.2017.08.015.
- 868 Müller, D., Walter, T.R., Schöpa, A., Witt, T., Steinke, B., Gudmundsson, M.T., and Dürig, T., 2017,
869 High-Resolution Digital Elevation Modeling from TLS and UAV Campaign Reveals Structural
870 Complexity at the 2014/2015 Holuhraun Eruption Site, Iceland: Frontiers in Earth Science, v.
871 5, <https://www.frontiersin.org/article/10.3389/feart.2017.00059> (accessed June 2022).
- 872 Nabyl, A., Dorel, J., and Lardy, M., 1997, A comparative study of low-frequency seismic signals
873 recorded at Stromboli volcano, Italy, and at Yasur volcano, Vanuatu: New Zealand Journal of
874 Geology and Geophysics, v. 40, p. 549–558, doi:10.1080/00288306.1997.9514783.
- 875 Nyamweru, C., 1990, Observations on changes in the active crater of Ol Doinyo Lengai from 1960 to
876 1988: Journal of African Earth Sciences (and the Middle East), v. 11, p. 385–390,
877 doi:10.1016/0899-5362(90)90017-9.
- 878 Oppenheimer, C., Bani, P., Calkins, J.A., Burton, M.R., and Sawyer, G.M., 2006, Rapid FTIR sensing
879 of volcanic gases released by Strombolian explosions at Yasur volcano, Vanuatu: Applied
880 Physics B, v. 85, p. 453–460, doi:10.1007/s00340-006-2353-4.
- 881 Pedersen, G.B.M., Belart, J.M.C., Óskarsson, B.V., Gudmundsson, M.T., Gies, N., Högnadóttir, T.,
882 Hjartardóttir, Á.R., Pinel, V., Berthier, E., Dürig, T., Reynolds, H.I., Hamilton, C.W., Valsson,
883 G., Einarsson, P., Ben-Yehosua, D., Gunnarsson, A., Oddsson, B., 2022. Volume, Effusion
884 Rate, and Lava Transport During the 2021 Fagradalsfjall Eruption: Results From Near Real-
885 Time Photogrammetric Monitoring. Geophys. Res. Lett. 49, e2021GL097125.
886 <https://doi.org/10.1029/2021GL097125>.
- 887 Reiss, M.C., Massimetti, F., Laizer, A.S., Campus, A., Rumpker, G., Kazimoto, E.O., 2023. Overview
888 of seismo-acoustic tremor at Oldoinyo Lengai, Tanzania: Shallow storage and eruptions of
889 carbonatite melt. J. Volcanol. Geotherm. Res. 107898.
890 <https://doi.org/10.1016/j.jvolgeores.2023.107898>.
- 891 Reiss, M.C., De Siena, L., and Muirhead, J.D., 2022, The Interconnected Magmatic Plumbing System
892 of the Natron Rift: Geophysical Research Letters, v. 49, p. e2022GL098922,
893 doi:10.1029/2022GL098922.
- 894 Rey, T., Leone, F., Defosse, S., Gherardi, M., and Parat, F., 2021, Volcanic hazards assessment of
895 Oldoinyo Lengai in a data scarcity context (Tanzania): Territorium, p. 69–81,
896 doi:10.14195/1647-7723_28-2_6.

- 897 Samsonov, S.V., 2019, User manual, source code, and test set for MSBASv3 (Multidimensional Small
898 Baseline Subset version 3) for one-and two-dimensional deformation analysis: Geomatics
899 Canada,.
- 900 Samsonov, S., and d'Oreye, N., 2012, Multidimensional time-series analysis of ground deformation
901 from multiple InSAR data sets applied to Virunga Volcanic Province: *Geophysical Journal*
902 *International*, v. 191, p. 1095–1108, doi:10.1111/j.1365-246X.2012.05669.x.
- 903 Schmid, M., Kueppers, U., Civico, R., Ricci, T., Taddeucci, J., and Dingwell, D.B., 2021, Characterising
904 vent and crater shape changes at Stromboli: implications for risk areas: *Volcanica*, v. 4, p. 87–
905 105, doi:10.30909/vol.04.01.87105.
- 906 Simons, B.C., Jolly, A.D., Eccles, J.D., and Cronin, S.J., 2020, Spatiotemporal Relationships between
907 Two Closely-spaced Strombolian-style Vents, Yasur, Vanuatu: *Geophysical Research Letters*,
908 v. 47, p. e2019GL085687, doi:https://doi.org/10.1029/2019GL085687.
- 909 Smets, B. et al., 2013, Detailed multidisciplinary monitoring reveals pre- and co-eruptive signals at
910 Nyamulagira volcano (North Kivu, Democratic Republic of Congo): *Bulletin of Volcanology*,
911 v. 76, p. 787, doi:10.1007/s00445-013-0787-1.
- 912 Snavely, N., Seitz, S.M., Szeliski, R., 2008. Modeling the World from Internet Photo Collections. *Int.*
913 *J. Comput. Vis.* 80, 189–210. https://doi.org/10.1007/s11263-007-0107-3.
- 914 Stamps, D.S., Saria, E., Ji, K.H., Jones, J.R., Ntambila, D., Daniels, M.D., and Mencin, D., 2016, Real-
915 time data from the Tanzania Volcano Observatory at the Ol Doinyo Lengai volcano in Tanzania
916 (TZVOLCANO): *Journal of Open Science Software*, doi:http://doi.org/10.5065fd6p849bm.
- 917 Stephens, K.J., and Wauthier, C., 2022, Spatio-temporal evolution of the magma plumbing system at
918 Masaya Caldera, Nicaragua: *Bulletin of Volcanology*, v. 84, p. 18, doi:10.1007/s00445-022-
919 01533-z.
- 920 Walter, T.R., Belousov, A., Belousova, M., Kotenko, T., and Auer, A., 2020a, The 2019 Eruption
921 Dynamics and Morphology at Ebeko Volcano Monitored by Unoccupied Aircraft Systems
922 (UAS) and Field Stations: *Remote Sensing*, v. 12, p. 1961, doi:10.3390/rs12121961.
- 923 Walter, T.R., Jousset, P., Allahbakhshi, M., Witt, T., Gudmundsson, M.T., and Hersir, G.P., 2020b,
924 Underwater and drone based photogrammetry reveals structural control at Geysir geothermal
925 field in Iceland: *Journal of Volcanology and Geothermal Research*, v. 391, p. 106282,
926 doi:10.1016/j.jvolgeores.2018.01.010.
- 927 Werner, C., Wegmüller, U., Strozzi, T., and Wiesmann, A., 2000, Gamma SAR and interferometric
928 processing software.: *Proceedings of the ers-envisat symposium*, v. 1620, p. 1620.
- 929 Westoby, M.J., Brasington, J., Glasser, N.F., Hambrey, M.J., and Reynolds, J.M., 2012, 'Structure-
930 from-Motion' photogrammetry: A low-cost, effective tool for geoscience applications:
931 *Geomorphology*, v. 179, p. 300–314, doi:10.1016/j.geomorph.2012.08.021.
- 932 Zorn, E.U., Walter, T.R., Johnson, J.B., and Mania, R., 2020, UAS-based tracking of the Santiaguito
933 Lava Dome, Guatemala: *Scientific Reports*, v. 10, p. 8644, doi:10.1038/s41598-020-65386-2.
- 934